

Laser-Induced Electron Emission from Arrays of Carbon Nanotubes

by

Parham Yaghoobi

B.A.Sc., The University of British Columbia, 2007

M.A.Sc., The University of British Columbia, 2009

A THESIS SUBMITTED IN PARTIAL FULFILLMENT OF
THE REQUIREMENTS FOR THE DEGREE OF

DOCTOR OF PHILOSOPHY

in

The Faculty of Graduate Studies

(Electrical and Computer Engineering)

THE UNIVERSITY OF BRITISH COLUMBIA

(Vancouver)

April 2012

© Parham Yaghoobi 2012

Abstract

Recently there has been growing interest in the interaction of light and nanomaterials, especially carbon nanotubes. Although there exist a large number of studies on the physical and chemical properties of nanotubes with various spectroscopic techniques, only a limited number of works have looked at this interaction for electron source applications. The work presented in this thesis demonstrates light-induced electron emission from arrays of nanotubes with a broad range of wavelengths and light intensities. I demonstrate that arrays of nanotubes have a quantum efficiency of $> 10^{-5}$ in the photoelectric regime, which is comparable to that of metal photocathodes such as copper. Nanotubes are also expected to have better operational lifetime than metals because of their complete chemical structure. I also demonstrate that, based on an effect called “Heat Trap”, a spot on the surface of a nanotube array can be heated to above 2,000 K using a low-power beam of light with a broad range of wavelengths from ultraviolet to infrared. Light-induced heating of a typical bulk conductor to electron emission temperatures requires high-power lasers. This is because of the efficient dissipation of heat generated at the illuminated spot to the surroundings, since electrical conductors are also typically excellent thermal conductors. I show that the situation can be drastically different in an array of nanotubes. This behaviour has far-reaching implications for electron sources. For example, the fabrication cost of light-induced electron sources can be significantly reduced since the nanotube-based cathode can be heated to thermionic emission temperatures with inexpensive, low-power, battery-operated handheld lasers as apposed to high-power or pulsed laser sources, which are currently required for metal cathodes. Arrays of nanotubes can also be shape engineered because of their sparse nature. I have demonstrated that the emission current density can

Abstract

be increased by a factor of 4 by densifying the array with a liquid-induced shrinkage that works by pulling the nanotubes closer together. The Implications of the findings reported in this thesis go beyond conventional electron-beam technologies. For instance, they could lead to novel devices such as thermionic solar cells, solar displays and new types of optical modulators and thermoelectrics.

Preface

The contributions from this thesis has led to the following publications and presentations:

Journal Papers

1. Parham Yaghoobi, Mario Michan, and Alireza Nojeh. Middle-ultraviolet laser photoelectron emission from vertically aligned millimeter-long multiwalled carbon nanotubes. *Applied Physics Letters*, 97(15):153119, 2010. (Part of Chapter 3)
2. Parham Yaghoobi, Mehran Vahdani Moghaddam, Mario Michan, and Alireza Nojeh. Visible-light induced electron emission from carbon nanotube forests. *Journal of Vacuum Science & Technology B*, 29(2):02B104, 2011. (Part of Chapter 4)
3. Parham Yaghoobi, Mehran Vahdani Moghaddam, and Alireza Nojeh. “Heat Trap”: Light-induced localized heating and thermionic electron emission from carbon nanotube arrays. *Solid State Communications*, 151(17):1105, 2011. (Part of Chapter 5)
4. Mehran Vahdani Moghaddam, Parham Yaghoobi, and Alireza Nojeh. Temperature-dependant quantum efficiency and transition from photoemission to thermionic emission in carbon nanotube arrays under low-power ultraviolet illumination, To be submitted. (Part of Chapter 6)

Conference Papers

1. Parham Yaghoobi, Mehran Vahdani Moghaddam, and Alireza Nojeh. Broadband-light-induced thermionic electron emission from arrays of carbon nanotubes using laser pointers. In The 55th International Conference on Electron, Ion, and Photon Beam Technology and Nanofabrication, Las Vegas, USA, May 2011. (Part of Chapter 7)
2. Parham Yaghoobi, Mehran Vahdani Moghaddam, and Alireza Nojeh. Increasing the current density of light-induced thermionic electron emission from carbon nanotube arrays. In The 24th International Vacuum Nanoelectronics Conference, Wuppertal, Germany, July 2011. (Part of Chapter 8)
3. Parham Yaghoobi, Mehran Vahdani Moghaddam, and Alireza Nojeh. Trapping Heat in a Conductor: Unusual Light-Induced-Heat Localization in Carbon Nanotube Forests. In Nanotube 2011 International Conference, Cambridge, United Kingdom, July 2011.

All of the chapters were written by the author with the assistance of Prof. Alireza Nojeh. All of the experiments except from the work presented in chapter 3 were conceived by the author, Dr. Mehran Vahdani Moghaddam and Prof. Alireza Nojeh and performed by the author and Dr. Mehran Vahdani Moghaddam with guidance from Prof. Alireza Nojeh. The author analyzed and interpreted all of the data and discussed it with Dr. Mehran Vahdani Moghaddam and Prof. Alireza Nojeh. The experiments of chapter 3 were conceived by the author and Prof. Alireza Nojeh and performed by the author. The results for this chapter were analyzed and interpreted by the author and discussed with Prof. Alireza Nojeh. The thesis is heavily based on articles resulting from the research. Chapters 3 to 8 are modified versions of these articles.

Table of Contents

Abstract	ii
Preface	iv
Table of Contents	vi
List of Figures	ix
Acknowledgements	xix
Dedication	xx
1 Introduction and Objective	1
1.1 Motivation	1
1.2 Electron Emission Mechanisms	1
1.2.1 Field-Electron Emission	1
1.2.2 Thermionic Electron Emission	2
1.2.3 Light-Induced Electron Emission	3
1.3 Carbon Nanotubes and their Use in Electron Emission	6
1.3.1 Carbon Nanotubes	6
1.3.2 Field-Emission from Carbon Nanotubes	6
1.3.3 Thermionic Emission from Carbon Nanotubes	6
1.3.4 Light-Induced Electron Emission	7
1.4 Objectives of this Research	8
2 Experimental Apparatus	11
2.1 Carbon Nanotube Forest Growth and Characterization	11

Table of Contents

2.2	Design and Assembly of an Ultra-High Vacuum Chamber . . .	13
2.3	Laser Setup	14
3	Middle-Ultraviolet Laser Photoelectron Emission from Vertically Aligned Millimetre-Long Multiwalled Carbon Nanotubes	17
3.1	Methodology	17
3.2	Results and Discussion	18
3.2.1	Stopping Voltage Test	20
3.2.2	Rotation Test	20
3.2.3	Linear Photoemission	21
3.2.4	Quantum Efficiency	22
3.2.5	Optical Absorption in Nanotube Forests	22
3.3	Summary	25
4	Visible-Light Induced Electron Emission from Carbon Nanotube Forests	27
4.1	Methodology	27
4.2	Results and Discussion	27
4.2.1	Region I	28
4.2.2	Region II	32
4.3	Summary	33
5	A “Heat Trap” Light-Induced Thermionic Electron Source Using Carbon Nanotube Arrays	35
5.1	Introduction	35
5.2	Methodology	35
5.3	Results and Discussion	37
5.3.1	Light-Induced Thermionic Emission with Low Power Laser	37
5.3.2	“Heat Trap” Mechanism	38
5.3.3	Modelling of the “Heat Trap” Mechanism	42
5.3.4	Experimental Fit to the Proposed Model for “Heat Trap”	46

Table of Contents

5.3.5	Applications	49
5.4	Summary	50
6	Temperature-Dependant Quantum Efficiency and Transition from Photoemission to Thermionic Emission in Carbon Nan- otube Arrays Under Low-Power Ultraviolet Illumination	52
6.1	Methodology	53
6.2	Results and Discussion	53
6.3	Summary	58
7	Broadband Light-Induced Thermionic Electron Emission from Arrays of Carbon Nanotubes using Laser Pointers	59
7.1	Methodology	60
7.2	Results and Discussion	61
7.3	Summary	65
8	Increasing the Current Density of Light-Induced Thermionic Electron Emission from Carbon Nanotube Arrays	66
8.1	Methodology	66
8.2	Results and Discussion	67
8.3	Summary	69
9	Conclusion	70
9.1	Contributions	70
9.2	Future Work	72
9.2.1	Solar Electron Source	73
9.2.2	Solar Cell	74
	Bibliography	75

List of Figures

1.1	Field-emission mechanism.	2
1.2	Optical field-emission happens due to the modulation of the barrier by the optical field (red arrows). Photo-field emission consists of the excitation of the electron to a higher energy level (blue arrow) and then tunnelling of the electron due to an externally applied field.	5
1.3	Thesis outline.	10
2.1	CVD apparatus consisting of a tube furnace and a quartz tube.	12
2.2	The manifold configuration where precise flows of the gases are mixed.	12
2.3	(a) Scanning electron micrograph of the side-wall of the CNT forest. (b) Zoomed-in image of the side-wall. It shows the overall alignment of the CNT forest. (c) Transmission electron micrograph of a single CNT in the forest. This image demonstrates that the CNTs in the forest are multi-walled.	13
2.4	CVD reactor consisting of two heating zones and flowmeters.	14
2.5	The UHV chamber, which is equipped with an XYZ stage with sub-micrometer resolution, electrical and optical fiber feedthroughs, a sapphire viewport, and a leak valve for controlling the chamber's pressure.	15
2.6	An argon laser, a solid state laser and a second harmonic generator provide us with multi-wavelength capabilities.	16

List of Figures

3.1	CNT forests were grown on 1 nm of iron and 10 nm of alumina. The laser illuminated the forest at an angle θ with respect to the axis of the CNTs. The scanning electron micrograph close-up of the side of the forest (inset) shows the overall aligned nature of CNTs in the forest.	18
3.2	Photoemission I-V characteristics of the CNT forest with and without the 266-nm laser (incident at 90° to the CNTs) with a typical anode spacing of ~ 3 mm from the top surface of the CNT forest (error bars are smaller than the graph markers and are masked by them). Inset: non logarithmic plot of the first 150 V. The current measurement error is about 10^{-13} A.	19
3.3	(a) Emission current versus angle of rotation (θ) for the CNT forest and the control device (catalyst on substrate, but no CNT). (b) Emission current from CNT forest versus the 266-nm laser power under a 100-V bias voltage.	21
3.4	The direction of electromagnetic wave propagation is along the y-axis and the z axis is illustrated by \times	23
3.5	Flowchart for calculating the magnitude of the Poynting vector of the incident electromagnetic wave.	24
3.6	The magnitude of the Poynting vector as it travels through a 1-micrometer-thick CNT forest (logarithmic scale). Inset: non logarithmic plot of the first 100 nm. Notice the stronger absorption of s-polarized light.	26
4.1	Schematic (not to scale) of the experimental configuration. The nanotube forest was grown on 1 nm of iron deposited on 10 nm of alumina. The laser irradiated the sidewall of the forest.	28

List of Figures

4.2	Emission current-voltage characteristics of the nanotube forest under different powers of: (a) 488-nm laser (the kinks on the 1400 mW curve are due to the stabilization electronics of the high power single mode operation of the argon laser) and (b) 532-nm laser. There are three distinct regions in the current-voltage characteristics.	29
4.3	Emission current as a function of the incident optical power for illumination by the 532-nm laser. Only 1 V of bias was applied for collection of electrons and there was no field-emission in this case. Inset shows the curve on linear scale.	29
4.4	Emission current as a function of the calculated temperature by the 532-nm laser. Only 1 V of bias was applied for collection of electrons and there was no field-emission in this case. The solid line shows the Richardson fit to the data.	31
4.5	Fowler-Nordheim plot corresponding to the data of Figure 4.2(a) and (b). Indicated are two different slopes on the (no laser) field-emission curve (slope I and II) and a third slope (slope III) on the low-laser-power curve at high fields. The ratio of slopes I and III for (a) is ~ 2.9 and for (b) is ~ 2.3	33
5.1	Schematic of the experimental apparatus where the laser is focused with a lens, placed outside of the vacuum chamber, on the sidewall of the nanotube forest through a sapphire viewport.	36

List of Figures

5.2	(a) Schematic of the device showing the laser spot on the sidewall of the carbon nanotube forest. An incandescent spot is observed as the intensity of the laser is increased. The top left inset demonstrates that the incandescent spot is localized to the position of the laser beam and does not spread as the laser intensity is increased. The top right inset shows a scanning electron micrograph of the sidewall of an actual carbon nanotube forest and the nanotubes' overall alignment. (b) The photo of the device with the incandescent spot. The laser light has been filtered out and the glow has been attenuated in order to image the spot using a CCD camera. The white dotted box is used to draw attention to the sidewall of the forest. The silicon chip, on which the nanotubes are grown, and the edge of the copper anode, which collects the emitted electrons, are also shown.	39
5.3	The measured emission current versus the laser power for several wavelengths (488 nm, 514 nm, and 532 nm) shows a non-linear increase. The behavior is very similar in all cases, consistent with broad spectral absorption of CNTs [1, 2]. The laser spot was $\sim 250 \mu\text{m}$ in radius. A collection voltage of 50 V was applied, which is below that needed for field-emission (dark current is below the measurement noise). There is a threshold (or turn-on) region where the intensity of the laser is high enough to cause localized temperature increase and electron emission.	40

List of Figures

5.4	The measured emission current as a function of emission spot temperature (at 532 nm) shows a trend similar to that predicted by the Richardson-Dushman equation. The laser spot had a radius of $\sim 250 \mu\text{m}$. The dotted curve shows the current as a function of the measured temperature, which was determined by fitting the black body spectrum to the spectrum of the incandescent spot. The solid line shows the prediction of the Richardson-Dushman equation, where an emission spot radius of $\sim 230 \mu\text{m}$ was chosen to obtain this fit. The error bars for the measured emission current are much smaller than the graph markers and therefore not seen.	41
5.5	Optical spectra of the incandescent spot. The blue lines are the measured spectra, corrected for the response of the coupling fiber, and the black lines are Planck's black body radiation fits. The corresponding temperatures is shown above each graph.	41
5.6	Measured emission current as the laser beam is defocused by moving the CNT sample along the axis of the laser beam. The emitted current slowly decreases as the laser spot becomes larger and then the CNT sample suddenly stops emitting electrons. This sudden stop of emission is the threshold of "Heat Trap" where the heat induced by the laser can now easily dissipate along the CNT as its thermal conductivity increases with reduced temperature.	42
5.7	(a) Drawing of the localized heated area on the nanotube forest. (b) Zoomed-in drawing of the heated area. (c) Drawing of the the cross section of the heated spot. (d) Zoomed-in drawing of the heated spot with arrows showing the direction of heat dissipation.	44

List of Figures

5.8 (a) Temperature as a function of laser intensity for an anisotropic material (i.e. nanotube forest) and a $\frac{1}{\alpha T + \beta T^2}$ thermal conductivity behaviour for different laser spot areas. (b) Temperature as a function of laser intensity for an isotropic material and a $\frac{1}{T}$ thermal conductivity behaviour. The curve remains the same for different laser spot areas (explained in text). The parameters used for this figure were: $\epsilon = 1$, $\Phi = 4.6$ eV, $L = 14$ μm , $T_{room} = 300$ K, and the depth for calculating A_{heat} of the anisotropic case was calculated to be ~ 50 nm. The input power has been corrected for the transparency of the sapphire viewport (85% at 532 nm). 45

5.9 Laser intensity threshold as a function of laser spot radius. The illustrated behaviour follows a $\frac{1}{r}$ trend. 47

5.10 Emission current as a function of laser power. The calculated data have been obtained by finding the temperature using the power equilibrium equation and using it in the Richardson-Dushman equation for thermionic emission. The solid red line shows the calculated emission current with using a constant value for the thermal conductivity, which provides a good fit at low emission current but diverges at high emission. On the other hand, the solid black line, which uses a $\frac{1}{\alpha T + \beta T^2}$ behaviour for the thermal conductivity provides a good fit. The parameters used for this Figure are: $r = 240$ μm , $\epsilon = 1$, $\Phi = 4.6$ eV, $L = 25.5$ μm , $T_{room} = 300$ K, and the depth for calculating A_{heat} of the anisotropic case was calculated to be ~ 50 nm. The input power has been corrected for the transparency of the sapphire viewport (85% at 532 nm). . . . 48

List of Figures

5.11	A 50 mW, battery-operated hand-held laser was capable of heating the sample enough for thermionic emission. The laser was focused onto the sidewall of the forest using a lens with a 15-cm focal length. The sample is inside of the high vacuum chamber seen on the left and placed close to the sapphire viewport. An emission current of $\sim 13 \mu\text{A}$ is recorded by the electrometer through an insulated BNC feedthrough by applying a collection voltage of 50 V. This experiment demonstrates that laser-activated thermionic cathodes do not have to rely exclusively on sophisticated high-power pulsed laser anymore - a laser pointer and potentially even integrated lasers may also work.	49
6.1	(a) Experimental setup where the laser is focused onto the CNT sidewall. (b) Laser spot on the CNT forest sidewall. . .	54
6.2	(a) Emission current as a function of power for low intensity laser. (b) Emission current as a function of power for high intensity laser.	54
6.3	Temperature as a function of laser intensity. The parameters for calculating the temperature for the solid lines were: $r = 240 \mu\text{m}$ for the larger spot size (black line) and $r = 65 \mu\text{m}$ for the smaller spot size (red line), $\epsilon = 1$, $\Phi = 4.652 \text{ eV}$, $L = 14 \mu\text{m}$, $T_{room} = 300 \text{ K}$, and the depth of the hot area for calculating A_{heat} was $\sim 50 \text{ nm}$	55

List of Figures

6.4	Emission current as a function of temperature. (Note that the two separate parts of the curve were obtained in two different experiments and should be considered separately.) The parameters for calculating the temperatures (square markers) using equation 5.1 were: $r = 240 \mu\text{m}$, $\epsilon = 1$, $\Phi = 4.652 \text{ eV}$, $L = 14 \mu\text{m}$, $T_{room} = 300 \text{ K}$, and the depth of the hot area for calculating A_{heat} was $\sim 50 \text{ nm}$. The parameters for calculating the current using the Fowler-DuBridge model (equation 1.6) were: $\alpha = 11e - 8$, $E_{photon} = 4.66 \text{ eV}$, and $\Phi = 4.652 \text{ eV}$. The input power was corrected for the transparency of the sapphire viewport (70% at 266 nm).	56
6.5	(a) Quantum efficiency as a function of power for low laser intensity. (b) Quantum efficiency as a function of power for high laser intensity. (c) Quantum efficiency as a function of temperature (Note that the two separate parts of the curve were obtained in two different experiments and should be considered separate).	57
6.6	Emission current as a function of temperature on the Richardson axis for UV and green lasers.	58
7.1	Schematic of the experimental apparatus using a laser pointer where the beam is focused with a lens, placed outside of the vacuum chamber, on the sidewall of the nanotube forest through a sapphire viewport.	60

List of Figures

7.2 Electron emission current as function of laser power for laser wavelengths of 405 nm, 532 nm, 658 nm, and 1064 nm. In all cases the laser was focused to a spot in the range of 200 - 600 μm in diameter. Since this emission process depends on the light intensity, the beam shape of the laser can greatly affect the emission current for a given laser power. In the 658 nm and 1064 nm cases, the laser beams were overall wider, less circular and more difficult to focus, and therefore more laser power was needed for electron emission. Insets: nonlogarithmic plot for each wavelength. 62

7.3 Electron emission current as a function of estimated temperature using a power equilibrium equation. The measured data follow the thermionic emission behaviour predicted by the Richardson equation. The minimum measurement limit with our experimental setup is tens of picoamperes. The parameters for calculating the temperatures (square dots) using equation 5.1 are: $r = 115 \mu\text{m}$, $\epsilon = 1$, $\Phi = 4.652 \text{ eV}$, $L = 80 \mu\text{m}$, $T_{room} = 300 \text{ K}$, and the depth for calculating A_{heat} was $\sim 50 \text{ nm}$ 63

7.4 Multiple laser beams with different wavelengths being focused onto a single spot. 64

7.5 Emission current as a function of temperature for different combinations of laser wavelengths. The parameters for calculating the temperatures (square dots) using equation 5.1 are: $r = 215 \mu\text{m}$, $\epsilon = 1$, $\Phi = 4.652 \text{ eV}$, $L = 14 \mu\text{m}$, $T_{room} = 300 \text{ K}$, and the depth for calculating A_{heat} was $\sim 50 \text{ nm}$ 64

7.6 (a) Emission current as a function of pressure. (b) Emission current as a function of time at a pressure of $\sim 5 \times 10^{-3} \text{ Torr}$. The laser had a wavelength of 532 nm, spot diameter of $\sim 200 \mu\text{m}$ and power of 50 mW. 65

List of Figures

8.1	(a) Experimental apparatus. (b) Image of the emission spot with the laser light filtered out. (c) Cross-section of the emission spot showing its diameter.	67
8.2	Scanning electron micrographs of as-grown (a) and densified (b) CNT arrays.	67
8.3	Emission current density vs. temperature for the as-grown and densified CNT arrays. (b) Emission current as a function of time for both cases.	68
8.4	(a) Emission current as a function of vacuum level for incident laser wavelength of 532 nm. (b) Emission current stability over time at a pressure of $\sim 5 \times 10^{-3}$ Torr.	68
9.1	Band diagram of a solar-cell configuration of nanotubes.	74

Acknowledgements

The work in this thesis would have not been possible without the help and support of many of colleagues specially my incredibly supportive and dedicated advisor, Prof. Alireza Nojeh, and our research associate, Dr. Mehran Vahdani Moghaddam, who worked step by step with me into late hours of the night.

I would like to thank the staff of the Nanofabrication Facility and the BioImaging Facility at the University of British Columbia for their help with fabrication and imaging of my devices. I would like to also thank Prof. Lukas Chrostowski and Prof. Nicolas Jaeger for giving me access to their optical equipments.

I would like to also acknowledge the financial support that I received from the Natural Sciences and Engineering Research Council of Canada through my Alexander Graham Bell Canada Graduate Scholarship and additional support from the department of Electrical and Computer Engineering at the University of British Columbia.

Dedication

I dedicate this work to my parents.

Chapter 1

Introduction and Objective

1.1 Motivation

Light induced electron emission, the process of emitting electrons using incident photons, has broad applications ranging from electron sources in accelerators [3] and free-electron lasers [4] to modern solar cells [5]. Photo-electron emitters can have high current densities [6], low beam emittance (high brightness) [7], and be operated in poor vacuum conditions. Also the ability of controlling the emission using a light source (for example a laser) makes such electron sources an attractive choice for a wide application base. For example, ultrafast pulsed electron sources have enabled time-resolved electron microscopy [8], which is used to characterize processes on the time scales of atomic phenomena [9].

1.2 Electron Emission Mechanisms

1.2.1 Field-Electron Emission

Field-electron emission (or field-emission) is an electron emission mechanism in which electrons are emitted from a material by applying an electric field to its surface (on the order of a few volts per nanometer or higher). This field is created by applying a voltage between the material and an anode, which will bend the vacuum barrier (Figure 1.1). If this field is high enough, the electrons in the material will face a narrow enough potential barrier to tunnel through.

This phenomenon was modelled by Fowler and Nordheim in 1928 [10, 11, 12], which is still in use for studying field-emitters. The emission current-density (J) of a field-electron emitter has the following form:

$$J = \frac{GF^2}{\Phi} \exp\left[\frac{-H\Phi^{\frac{3}{2}}}{F}\right], \quad (1.1)$$

where $G = \frac{e^3}{8\pi h}$, $H = \frac{8\pi\sqrt{2m}}{3he}$, and e , h , and m are the fundamental constants of

1.2. Electron Emission Mechanisms

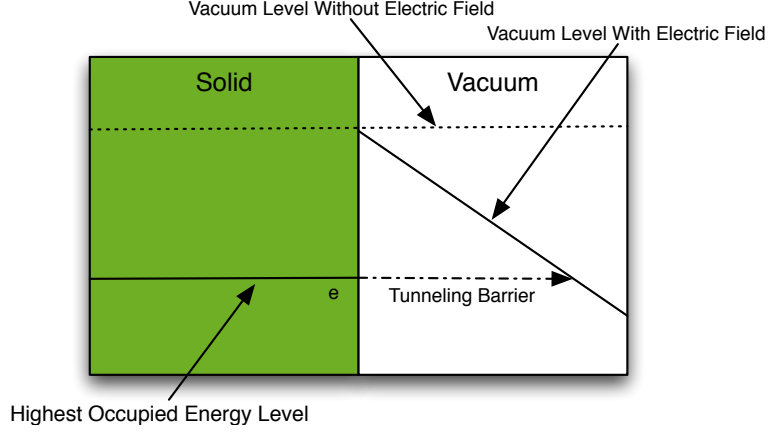


Figure 1.1: Field-emission mechanism.

the charge of an electron, Planck’s constant, and the mass of an electron, respectively. F is the applied electric field and Φ is the workfunction of the material. This general form of the Fowler-Nordheim equation is derived on the assumption that the emission occurs from a flat metallic surface. For sharp emitters such as Spindt cathodes [13] or carbon nanotube emitters [14], the local field at the emission spot is higher than that of a flat metal surface since the geometry of the emitter leads to strong field enhancement. In order to incorporate this effect a “field enhancement factor”, β , is introduced into the Fowler-Nordheim equation, which gives the equation the following form:

$$J = \frac{G(F\beta)^2}{\Phi} \exp\left[\frac{-H\Phi^{\frac{3}{2}}}{F\beta}\right]. \quad (1.2)$$

1.2.2 Thermionic Electron Emission

Thermionic emission is another electron emission mechanism, where the electrons are excited to escape the material through heating. The emitter is usually heated resistively and these type of emitters are the most commonly used electron sources in most applications. They are easy to fabricate (for example, a tungsten wire) and they can also operate in poor vacuum conditions. This emission mechanism was first empirically modelled by Richardson in 1901 [15]. The current form of Richardson’s equation is:

$$J = A_G T^2 \exp\left[\frac{-\Phi}{kT}\right], \quad (1.3)$$

1.2. Electron Emission Mechanisms

where J is the current density, A_G is Richardson's constant, T is temperature, k is Boltzmann's constant, and Φ is the work function of the material. When better models for electrons were developed after Richardson's work, Richardson's constant was theoretically derived to be $A_G = \frac{4\pi m k^2 e}{h^3} \approx 1.2 \text{Am}^{-2}\text{K}^{-2}$.

Schottky Electron Emission

Thermionic emission can also occur under a high applied electric-field, which creates an emission mechanism where the high electric-field behaves as a lowering of the workfunction of the thermionic process. This process is known as the Schottky electron emission and is modelled by Richardson's equation with the following form:

$$J = A_G T^2 \exp\left[-\frac{(\Phi - E_{Schottky})}{kT}\right], \quad (1.4)$$

where $E_{Schottky} = \sqrt{\frac{e^3 F}{4\pi\epsilon_0}}$. This emission process is not the focus of this thesis.

1.2.3 Light-Induced Electron Emission

There are four possible mechanisms of light induced electron emission from a material, namely photoemission, optical field-emission, photo field-emission, and thermionic emission.

Photoemission

Photo-electron emission (or photoemission) is a process by which an electron escapes a material by absorbing enough energy from a photon (to overcome the work function of the material). The simplest model for this emission mechanism is:

$$I = \frac{e}{h\nu} Q_E P_{laser}, \quad (1.5)$$

where I is the emission current, Q_E is the quantum efficiency (number of electrons emitted divided by the number of photons incident on the material), P_{laser} is the laser power and ν is the frequency of light. The quantum efficiency has been suggested to be proportional to $(h\nu - \Phi)^2$ [16]. The current state-of-the-art photocathodes have quantum efficiencies of $>10\%$. These photocathodes are a mixture of multilayer semimetals and alkalis, in particular cesium. However, these materials are highly sensitive and have to be made and operated in ultra-high vacuum (better than 10^{-10} Torr) and have a short operating life time. Metal photocathodes, on the other hand, are more robust and can be operated at lower vacuum conditions

1.2. Electron Emission Mechanisms

($\sim 10^{-6}$ Torr); however, they have much lower quantum efficiencies; for example, a copper photocathode has a quantum efficiency of $\sim 10^{-5}$ for 266-nm light [17].

Temperature plays a significant role in photoemission and this effect has been previously modelled by Fowler in 1931 [18] and has the following form:

$$I = 2e\alpha \frac{P_{laser}}{E_{photon}} \frac{U\left(\frac{E_{photon}-\Phi}{kT}\right)}{U\left(\frac{\Phi}{kT}\right)} \quad (1.6)$$

where I is the emission current, e is the charge of an electron, α is the absorption coefficient, k is Boltzmann's constant, T is the temperature, E_{photon} is the photon energy of the light, Φ is the workfunction of the material, $\frac{P_{laser}}{E_{photon}}$ is the number of photons per unit time, and $\frac{U\left(\frac{E_{photon}-\Phi}{kT}\right)}{U\left(\frac{\Phi}{kT}\right)}$ is the ratio between the number of available electrons due to photo excitation with momentum perpendicular to the surface of the metal and total number of electrons with momentum perpendicular to the surface of the metal. $U(x)$ has the form of $U(x) = \int_{\infty}^x \ln(1 + e^y) dy$ with no analytical solution; however, a parametric solution within 1% accuracy can be found in Ref. 19.

Optical Field-Emission

Optical field-emission happens when the electric field of a light source couples to the vacuum barrier (Figure 1.2) and modulates the barrier. If the intensity of the light is high enough the modulated potential barrier can become small enough for electrons to tunnel through during a portion of the optical cycles. This electron emission process was initially proposed by Hagmann [20] and is usually modelled by estimating the instantaneous magnitude of the electric field of the incoming light and using the Fowler-Nordheim equation (discussed in section 1.1). This process can only occur when the polarization of light is perpendicular to the emitter surface. Although this process has been used for modelling ultrafast pulsed electron source experiments [21], its validity is not entirely clear and some recent works attribute the emission mechanism due to ultrafast pulsed lasers to a multi-photon emission process [22, 23].

Photo field-emission

Photo field-emission is a process where the incoming photons do not have enough energy to make the electrons overcome the work function of the material. Instead, they excite the electrons to a higher energy level in the material and effectively

1.2. Electron Emission Mechanisms

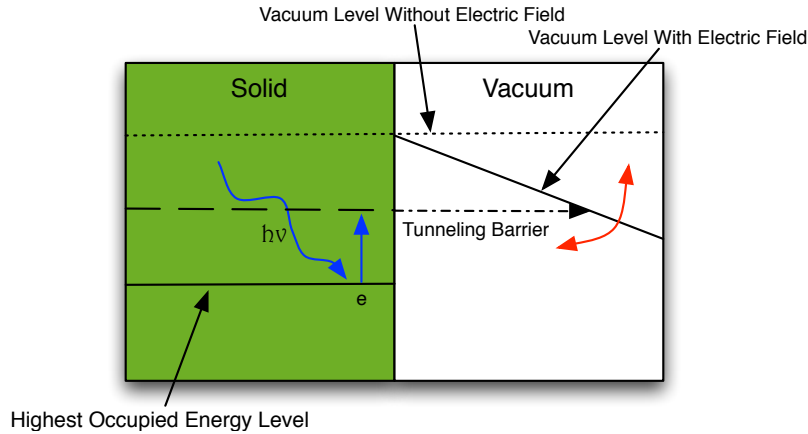


Figure 1.2: Optical field-emission happens due to the modulation of the barrier by the optical field (red arrows). Photo-field emission consists of the excitation of the electron to a higher energy level (blue arrow) and then tunnelling of the electron due to an externally applied field.

reduce the potential barrier that electrons, within the material, face. As a result electrons can tunnel through the barrier at a much lower field than in the absence of photons (Figure 1.2). This mechanism can also be modelled using the Fowler-Nordheim equation by reducing the work function of the material (Φ in equation 1.2) by the photon energy of the incident light. This process is commonly used in sharp electron emitters (for example, sharp metal needles [7]).

Light-Induced Thermionic Emission

As mention in section 1.2.2, the most common way of heating a material to thermionic emission temperatures is through resistive heating; however, the material can also be heated with a beam of laser, although it requires very high laser intensities. For example, the laser intensity required for electron emission from a tungsten needle is $\sim 10^{11} \text{ Wm}^{-2}$ [24], which is close to the laser ablation point for tungsten. This is because good electrical conductors are also good heat conductors; therefore, much of the absorbed energy from the laser is dissipated to a larger area and only a small portion of the energy contributes to the heating of the emission spot. Light-Induced thermionic emission can also be modelled using Richardson's equation (equation 1.4). It should be noted that there are a limited number of materials that can be used as a thermionic source since the temperature required for emission

is usually greater than the melting point of most materials.

1.3 Carbon Nanotubes and their Use in Electron Emission

1.3.1 Carbon Nanotubes

Carbon nanotubes (CNTs) consist of one or more rolled layers of graphene, which is a sheet of carbon atoms with a thickness of one atom arranged in a hexagonal lattice like a chicken wire [25]. The chemical bond between the neighbouring atoms in a CNT is stronger than the bonds found in diamond, which provides nanotubes with their unique strength. Thus, CNTs are among the strongest and stiffest materials known. Combined with their low density of 1.3-1.4 g cm⁻³, this makes them suitable for high-strength-to-weight-ratio applications. Based on their geometry, namely its chirality and diameter, a CNT can be metallic or semiconducting. With lengths of up to centimetres demonstrated experimentally, CNTs have very high aspect ratios, virtually making them one-dimensional. Electronic transport in CNTs can be ballistic over distances of several micrometer at room temperature. Together with their ability to withstand current densities of up to 10⁹ Acm⁻² (orders of magnitude higher than traditional copper and silver wires), this makes CNTs very attractive for electronic applications.

1.3.2 Field-Emission from Carbon Nanotubes

The high aspect ratio of nanotubes made them an immediate candidate for field-emission emitters after their discovery. This is because of the high field-enhancement factor that they can achieve due to their geometry, in addition to a small emission spot. A great amount of research has been conducted in this area and I have previously written a review paper on this topic [26]. However, this is not the emission mechanism of interest in this thesis and will not be discussed further.

1.3.3 Thermionic Emission from Carbon Nanotubes

One of the earliest reports on thermionic emission from CNTs was that of Cox *et al.* who resistively heated a single multi-walled carbon nanotube (MWNT) [27]. Since CNTs are expected to have high thermal conductivity, they attributed their observation of thermionic emission to the defective nature of their MWNT, which must have a poor thermal conductivity. Two subsequent works that reported thermionic

emission consist of resistively heating up single-walled, double-walled, and multi-walled CNT bundles [28] and CNT yarns [29], and measuring their work functions. Wei *et al.* also used thermionic emission to measure the difference in work function of CNT yarns and sheets [30]. In all these works, Richardson's equation (equation 1.4) was used to analyze the measured results.

1.3.4 Light-Induced Electron Emission

There are a limited number of works that demonstrate light-induced electron emission from CNTs. Photoemission and light-induced thermionic emission from CNTs are the two mechanisms that have so far been investigated. The next two sections provide an overview of the majority of the literature in these two topics.

Photoemission

The main focus of previous research in photoemission from CNTs has been on photoemission spectroscopy, typically performed with photon energies of greater than 10 eV, which is much higher than the work function of CNTs ($\sim 4\text{-}5$ eV), for studying the electronic structure and binding energies [31, 32]. The study of photoemission from CNTs with photon energies of a few eV for device applications (i.e. photocathodes) has been limited. Nojeh *et al.* demonstrated photoemission from sparse collections of single-walled nanotubes (SWNTs) lying on a substrate using a 266-nm (4.66-eV) continuous-wave laser [33]. It appeared that the absorption cross-section of a SWNT is larger than its geometrical cross-section, suggesting efficient absorption mechanisms based on optical antenna effects. Wong *et al.* used pulsed lasers (at 532 nm, 355 nm, and 266 nm) to observe photoemission from a mat of horizontal, randomly distributed MWNTs on a surface, with lengths in the 5-10 μm range [34]. At 266 nm they observed photoemission with a quantum efficiency of $\sim 10^{-7}$ under a collection electric field of $1.67\text{ V}\mu\text{m}^{-1}$, which is in the same order of magnitude as fields needed for field-emission from CNTs [35]. Hudanski *et al.* demonstrated a photocathode that uses silicon photodiodes to control electron emission from MWNT field-emitters [36]. Westover *et al.* reported photo- and thermionic emission from potassium-intercalated carbon nanotube arrays [37].

Light-Induced Thermionic Heating of Carbon Nanotubes

Thermionic emission through laser heating was observed in the work of Wong *et al.* who heated up a mat of randomly distributed, horizontal MWNTs using pulsed

lasers at 532 nm and 355 nm [34]. One of the earliest works on field-emission from carbon nanotubes used a focused beam of laser to control the temperature of an individual nanotube while measuring its field emission properties [38]. Others have investigated the effect of laser irradiation on CNTs. Bassil *et al.* examined the effect of laser heating on Raman spectra. They observed more effective heating of CNTs at the 488 nm laser wavelength than at 647 nm [39]. Nakamiya *et al.* investigated the damage threshold of MWNT films using pulsed lasers at the first two harmonics of a Nd:YAG laser ($\lambda = 1064$ nm and 532 nm) and a pulsed KrF excimer laser ($\lambda = 248$ nm) [40, 41]. They measured the minimum energies (and calculated the corresponding temperatures) that damage and graphitize MWNT films. A localized heating and glow of nanotube arrays under an ultra-violet laser focused to a submicron spot has been reported in Ref. 42. The glow spectrum in that case exhibited photoluminescence behaviour rather than black body radiation.

1.4 Objectives of this Research

As mentioned earlier, the ability to induce and control electron emission with a light source has a wide range of applications. Nanotubes, because of their robust and sharp structure, are great candidates for material for electron sources. However, there are only a limited number of works on nanotubes as light-induced electron sources, even though nanotubes have interesting optical properties that differ significantly from conventional bulk materials such as sharp optical transitions due to Van Hove singularities, or high optical absorption in a nanotube forest, which is close to an ideal black body. The objective of this thesis is to investigate light-induced electron emission from nanotubes using continuous-wave (CW) lasers with a broad range of wavelengths and light intensities. Although the technological motivation behind this research was the continuous need for new and improved light-induced electron sources, the expectation that the rich physics of interaction of light with nanotstructures should lead to interesting new phenomena provided another strong motivation for this largely exploratory work.

There are four controllable parameters that are involved in CW laser-induced electron emission, namely, laser wavelength, laser power, laser spot size, and applied collection electric field. To investigate laser-induced electron emission from CNTs, all of these parameters should be considered. Figure 1.3 illustrates the outline of this thesis based on these three parameters in a graphical form. Electron emission as a function of applied electric field, which is field-emission, is not the mechanism of interest in this thesis as mentioned before; therefore, all of the work carried

1.4. Objectives of this Research

out in this thesis (except from photo field-emission discussed in section 4.2.2) was conducted with a very low applied electric field, which is for collecting electrons at the anode (maximum of ~ 15 V/mm) and is orders of magnitude below the electric field required for field-emission from CNTs.

Chapter 2 provides a description of all the equipment that were designed and built for performing the experiments and the following chapters describe the observations, analysis and conclusions of different combinations of parameters. For example, chapter 3 describes photoemission from CNTs using a 266-nm laser with very low laser intensity and chapters 4 and 5 explain laser-induced thermionic emission with visible lasers with higher light intensities. In chapter 5, the observed heated area is very localized on the CNTs and this “Heat Trap” phenomenon, which increases the temperature of the nanotubes to the thermionic regime with low laser intensities, is very unusual and has not been observed in bulk metals such as tungsten.

1.4. Objectives of this Research

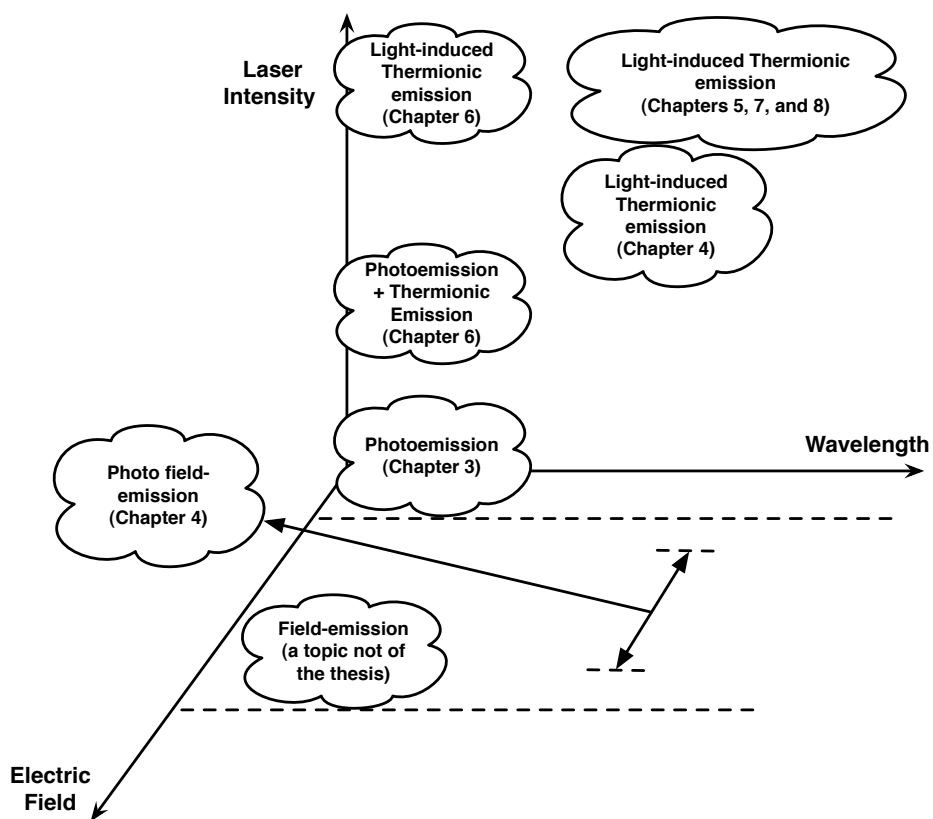


Figure 1.3: Thesis outline.

Chapter 2

Experimental Apparatus

2.1 Carbon Nanotube Forest Growth and Characterization

In order to study nanotube electron sources experimentally, I have built and characterized two chemical vapour deposition (CVD) reactors with two recipes for growing arrays of aligned carbon nanotubes (nanotube forest) and helped with designing and assembling an ultra-high vacuum chamber, which is an ideal environment for characterizing electron emission from carbon nanotubes.

The CVD apparatus is shown in Figure 2.1. It consists of a quartz tube that is heated with a tube furnace. There are four available lines for gases (ethylene, methane, hydrogen, and argon) that can be mixed together through a manifold (Figure 2.2). The flow of each gas can be controlled accurately ($\pm 10 - 20$ sccm for methane, hydrogen, ethylene, and argon) using a thermal mass flow controller. Various combinations of these gases can be used in different recipes for growing carbon nanotubes.

The recipe for growing millimetre long forests of CNTs is based on a combination of the recipes proposed by Hata *et al.* [43], Zhang *et al.* [44], and Chakrabarti *et al.* [45]. As catalyst for CNT forest growth, 10 nm of Alumina and 1-2 nm of iron were evaporated successively on a highly p-doped silicon wafer. A typical growth entails heating the sample up to 750 °C under a flow of 400 sccm of Ar. The flow is maintained at 750 °C for 15 min before the sample is annealed for 3 minutes under 500 sccm of H₂ and 200 sccm of Ar. Immediately after annealing, a flow of 140 sccm of C₂H₄ is introduced for an hour to grow the CNT forests. The sample is then cooled down under a flow of 400 sccm of Ar. As can be seen from the scanning electron micrograph of the side of the forest (Figure 2.3), the CNTs are overall aligned in the vertical direction.

The second generation CVD system consists of two heating zones (the tube furnace and substrate heater shown in Figure 2.4). As the gas flows through the system, the first heating zone (i.e. the tube furnace) breaks down C₂H₄ and H₂

2.1. Carbon Nanotube Forest Growth and Characterization

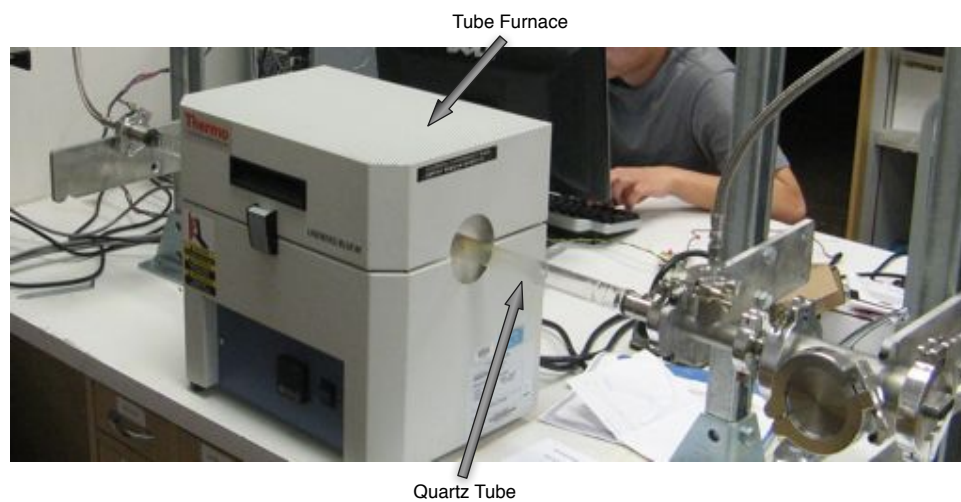


Figure 2.1: CVD apparatus consisting of a tube furnace and a quartz tube.

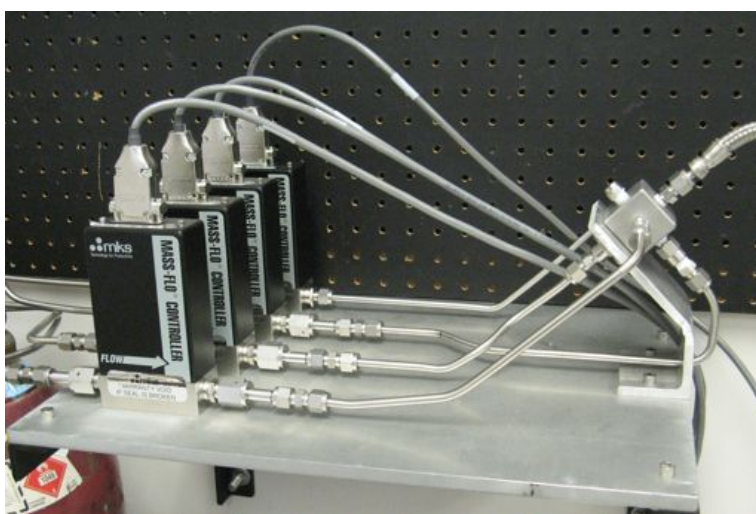


Figure 2.2: The manifold configuration where precise flows of the gases are mixed.

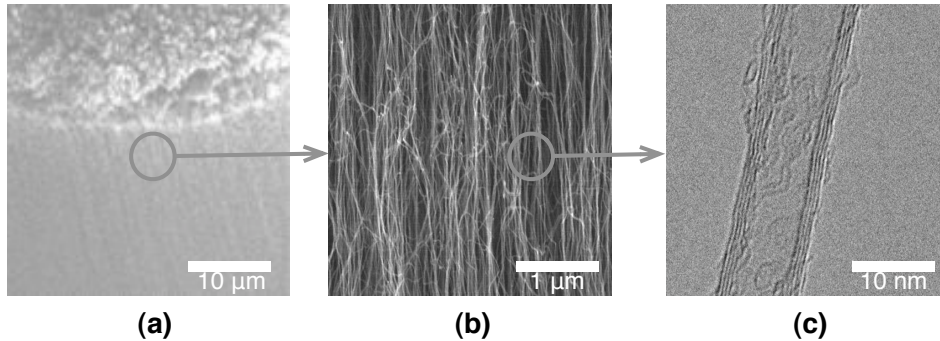


Figure 2.3: (a) Scanning electron micrograph of the side-wall of the CNT forest. (b) Zoomed-in image of the side-wall. It shows the overall alignment of the CNT forest. (c) Transmission electron micrograph of a single CNT in the forest. This image demonstrates that the CNTs in the forest are multi-walled.

and the second heating zone (i.e. the substrate heater) activates the catalyst and enables growth. By decoupling these two processes with two heating zones, better control over the growth can be achieved. The recipe for this growth is very similar to the work by Hart *et al.* [46]. The catalyst and the gases used for the growth are the same as in the first CVD reactor, only the flow rates and durations are different. For a typical growth, the tube furnace is heated to 850 °C under 400 sccm of Ar and then the substrate heater is heated to about 800 °C under the same flow rate of Ar. The sample is then annealed for 5 minutes under 140 sccm of Ar and 400 sccm of H₂. The growth is then initiated by decreasing the flow of Ar to 100 sccm, maintaining the flow of H₂, and introducing 140 sccm of C₂H₄. The CNT arrays can reach a height of ~1 mm after about an hour of growth.

2.2 Design and Assembly of an Ultra-High Vacuum Chamber

An ultra-high vacuum (UHV) chamber provides an environment with pressures as low as 10^{-12} Torr depending on the cleanliness of the chamber. This pressure translates into a mean free path of 100,000 km for gas molecules. This is an ideal environment for characterizing CNT electron emitters because it tremendously slows down the deposition rate of nitrogen or other atoms or molecules that could greatly affect the electronic structure of CNTs and, therefore, their electron

2.3. Laser Setup

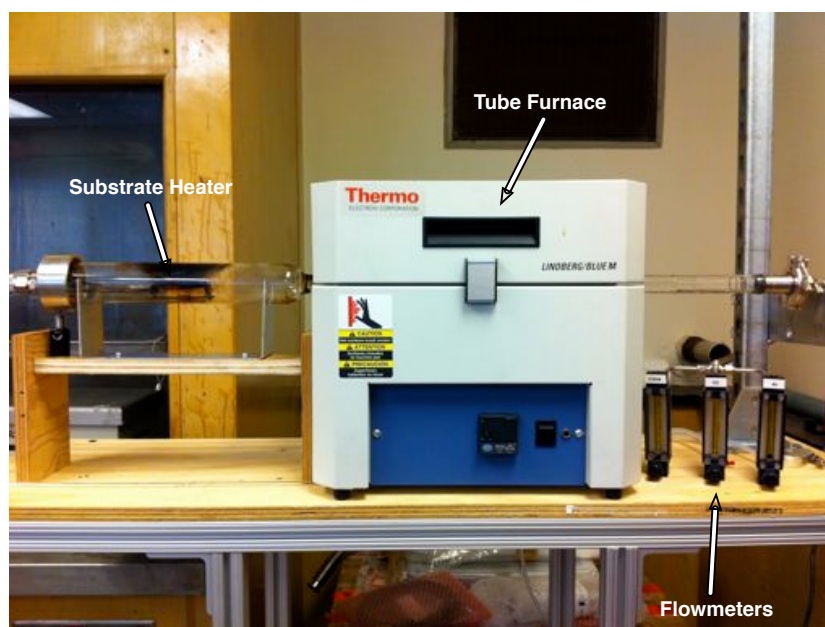


Figure 2.4: CVD reactor consisting of two heating zones and flowmeters.

emission behaviour. For the experiments presented in this thesis a vacuum pressure between 10^{-7} to 10^{-9} Torr was achieved with the system. Figure 2.5 is a picture of our UHV chamber, which I have helped design and assemble. This chamber is equipped with an XYZ stage with sub-micrometer resolution, electrical and optical fiber feedthroughs, a sapphire viewport, and a leak valve for controlling the chamber's pressure. A typical experiment would have the incoming laser beam focused with a lens through the viewport and onto the CNT sample, which is placed inside the chamber. The current emission characteristics were measured with a Keithley 6517A electrometer through the electrical feedthrough.

2.3 Laser Setup

We have a Coherent Verdi V-5 laser capable of producing up to 5 W of continuous-wave, 532-nm light, a Spectra-Physics Beamlok 2060-10S argon laser capable of single mode operation at different wavelengths (with high power modes at 476.5 nm, 488 nm, 496.5 nm, and 514.5 nm), and a second-harmonic generator for producing 266-nm ultraviolet using the Verdi laser. This configuration presents us with a wide variety of laser lines, which is crucial for this study. Operating each of these lasers

2.3. Laser Setup

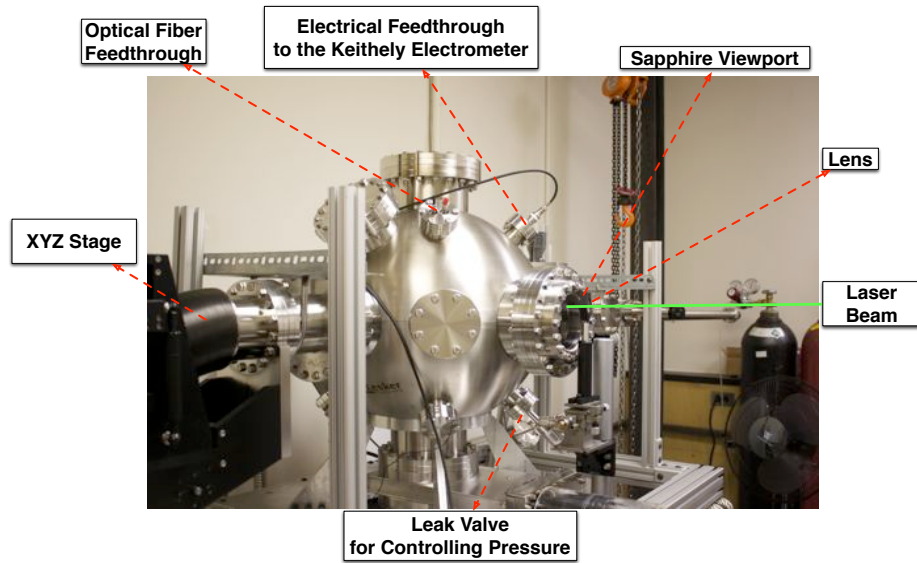


Figure 2.5: The UHV chamber, which is equipped with an XYZ stage with sub-micrometer resolution, electrical and optical fiber feedthroughs, a sapphire viewport, and a leak valve for controlling the chamber's pressure.

has its own challenges as each requires precise tuning and calibration before any operation. A picture of the laser setup is shown in Figure 2.6

2.3. Laser Setup

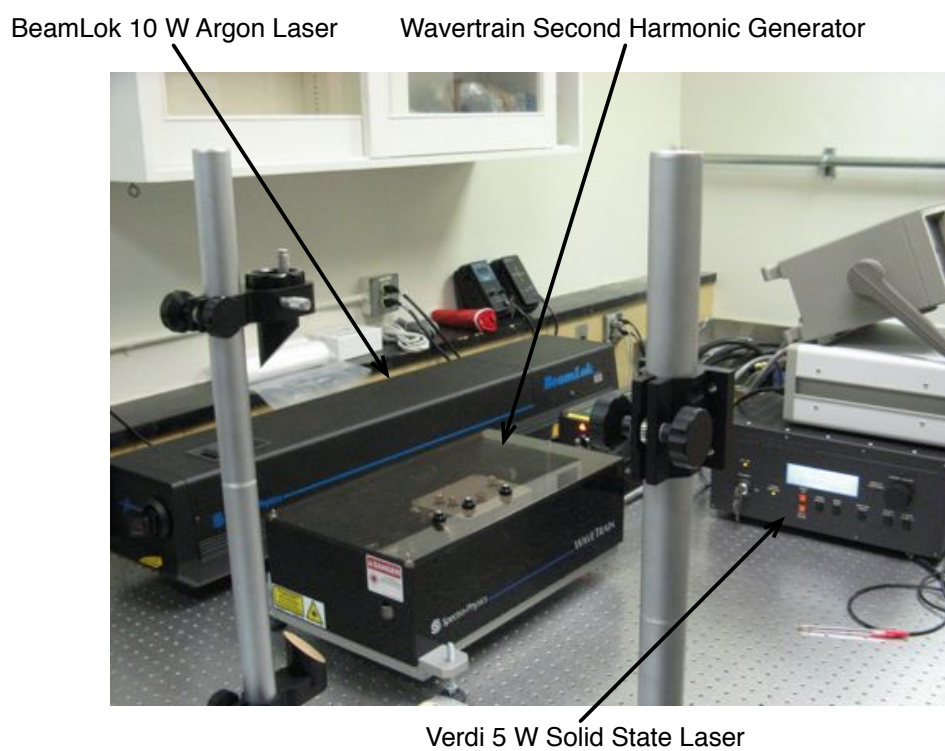


Figure 2.6: An argon laser, a solid state laser and a second harmonic generator provide us with multi-wavelength capabilities.

Chapter 3

Middle-Ultraviolet Laser Photoelectron Emission from Vertically Aligned Millimetre-Long Multiwalled Carbon Nanotubes

3.1 Methodology

The nanotube sample was placed in a custom-made holder, where it served as the cathode. A metallic wire, placed at a distance of ~ 3 mm from the top surface of the CNT forest, served as the anode/collector. The sample holder was placed on a rotating arm in a high-vacuum chamber pumped down to $\sim 10^{-8}$ Torr using a dry (turbomolecular) pump. Given the workfunction of the CNT forest, which is in the 4.5 - 5 eV range, a 532-nm laser (Coherent Verdi V-5) was used to generate a continuous wave 266-nm (or 4.66 eV of photon energy) ultraviolet (UV) beam using a frequency doubler (Spectra-Physics Wavetrain). We expect that a photon energy of 4.66 eV would be higher than the workfunction of some of CNTs in the forest. This beam was then guided into the vacuum chamber through a sapphire viewport (UV transparency of 70%) and onto the CNT forest (Figure 3.1). To apply a collection voltage and measure the collected current at the cathode, a Keithley 6517A source/electrometer was used.

A version of this chapter has been published in Applied Physics Letters. [47]

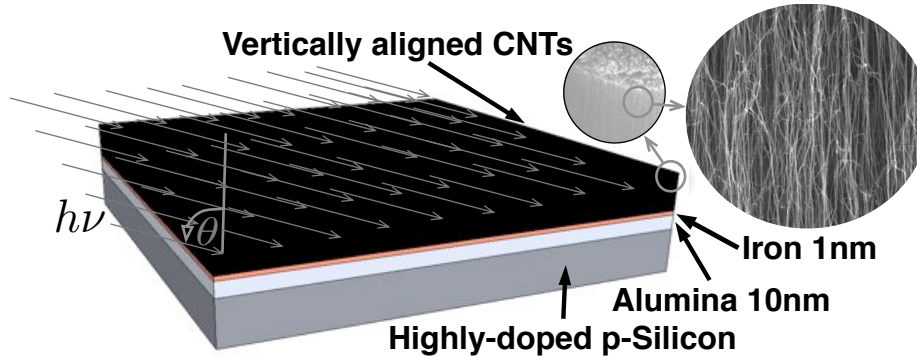


Figure 3.1: CNT forests were grown on 1 nm of iron and 10 nm of alumina. The laser illuminated the forest at an angle θ with respect to the axis of the CNTs. The scanning electron micrograph close-up of the side of the forest (inset) shows the overall aligned nature of CNTs in the forest.

3.2 Results and Discussion

Figure 3.2 illustrates the I-V characteristics of the CNT forest both with 100 mW of continuous-wave (CW) 266-nm laser (incident at an angle of $\theta = 90^\circ$, i.e. illuminating the side of the forest) and without laser. The photoemission current quickly ramps up to its maximum at a collection field of $\sim 0.33 \text{ Vmm}^{-1}$ (Figure 3.2 inset), which is far below the threshold of field-emission. This increase in current as a function of applied voltage is mainly due to the location and the shape of the anode. The thin wire placed above the forest is not wide enough or in the path of the trajectory of the photoemitted electrons in order to collect most of them. Therefore, the increase in the applied voltage attracts the electrons toward the anode, which increases the number of collected electrons. Up to a voltage of $\sim 600 \text{ V}$ (collection field of $0.2 \text{ V}\mu\text{m}^{-1}$), no field-emission is observed and an almost constant photoemission current of $\sim 30 \text{ nA}$ is obtained. At higher voltages, we start to see field-emission from the forest and, even without light, there is significant current.

To confirm that (at least the majority of) photoemission is occurring from the CNTs and not the substrate, two experiments were carried out. First, we conducted a stopping voltage test, where we applied a negative bias to the anode until no current was measured through it. Then, we performed a rotation test, in which we changed the angle of incidence of light. Both tests were carried out on two samples, one including a CNT forest and another with only the Si substrate

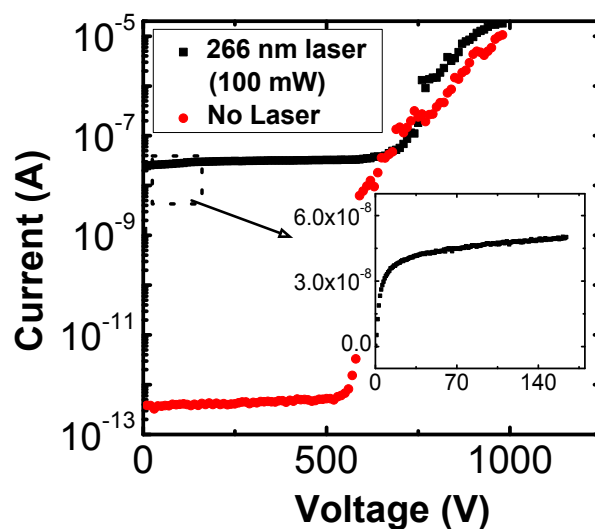


Figure 3.2: Photoemission I-V characteristics of the CNT forest with and without the 266-nm laser (incident at 90° to the CNTs) with a typical anode spacing of ~ 3 mm from the top surface of the CNT forest (error bars are smaller than the graph markers and are masked by them). Inset: non logarithmic plot of the first 150 V. The current measurement error is about 10^{-13} A.

and the catalyst (alumina/iron).

3.2.1 Stopping Voltage Test

In principle, the stopping voltage test can also reveal the work function of the emitting material, since the stopping voltage corresponds to the kinetic energy of the emitted electrons, which is the difference between the incident photon energy and the work function. However, this is a rather simplistic view based on neglecting the energy distribution of the electrons, the emission of phonons and effects such as two-photon absorption. In addition, it assumes no contact resistance at the cathode and anode. Therefore, in practice we were not able to measure the work function on an absolute scale. However, this test is still useful since the difference between the two samples is only the CNT forest and, if the measured stopping voltage is different in the two cases, then one may conclude that the emitted electrons are originating from materials with different work functions. Indeed, the measured stopping voltages were considerably different: for the sample with CNT forest, we measured a stopping voltage of ~ 0.02 V, whereas for the sample with catalyst only, we measured ~ 0.2 V. This method was also used to ensure that the emitted electrons from the CNTs are due to photoemission and not a thermionic process (laser heating of the CNTs): The intensity of the laser was increased while the anode was biased at the stopping voltage and no increase in emitted current was measured. The laser intensity required for measurable thermionic emission with the 266-nm laser is much higher, which is discussed in chapter 6. However, one could expect a slight temperature increase as the laser power is increased.

3.2.2 Rotation Test

In the rotation test, we gradually changed the direction of different samples with respect to the angle of incidence of the laser beam, while keeping the applied voltage and the distance between the anode and cathode constant (the anode also rotated with the sample) in order to keep the collection field constant. The results are shown in Figure 3.3(a). The photoemission current decreases as we rotate the sample with only Si wafer and catalyst, as opposed to the behaviour of the device containing the CNT forest (this was tested on two different nanotube forests). This difference in behaviour is yet another indication that the electrons are being emitted from different materials in the two cases (in one case from the substrate/catalyst and in the other from the nanotubes).

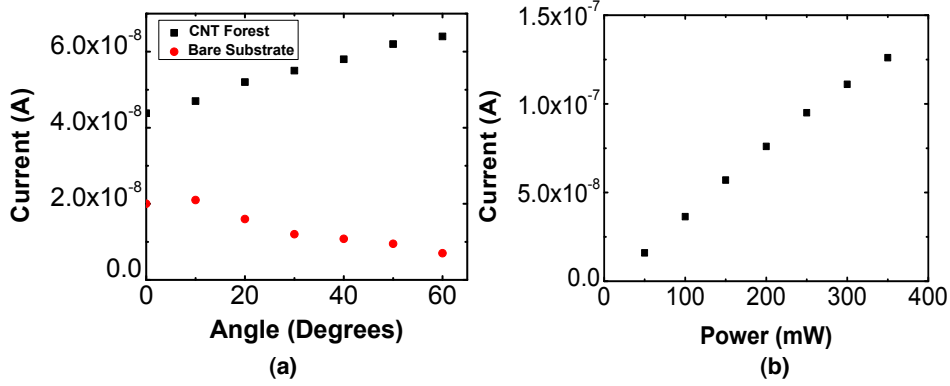


Figure 3.3: (a) Emission current versus angle of rotation (θ) for the CNT forest and the control device (catalyst on substrate, but no CNT). (b) Emission current from CNT forest versus the 266-nm laser power under a 100-V bias voltage.

The increase in photoemission current as the angle θ is increased may be explained as follows: For small θ , the laser illuminates the forest mainly from the top, i.e. light only hits the tips of the nanotubes. Given the sparse nature of the forests (our characterization reveals that they are more than 85% empty space), only a small portion of the light is expected to be absorbed by the nanotubes near the top surface. Moreover, in this case the electric field of light is mostly in the direction perpendicular to the nanotube axis. As the angle θ is increased and the forest is illuminated more from the side, the effective area covered by nanotubes in the beam path grows larger because the beam will start to cover the sidewall of the nanotubes as appose to just their tips. In addition, the component of the laser's electric field along the tube axis grows with θ , favouring stronger emission. In the case of the sample with only catalyst (11 nm in thickness), increasing θ decreases the photon density on the surface area being illuminated, which reduces the emission current.

3.2.3 Linear Photoemission

Figure 3.3(b) illustrates an almost linear behaviour in the photoemission current from the CNT forest versus laser power. This suggests that emission is mainly through helping electrons overcome the work function barrier, rather than non-linear effects such as optical field-emission (where the tunnelling barrier width is modulated by the light), which could happen at higher intensities.

3.2.4 Quantum Efficiency

In our experiments, approximately 20% of the laser beam covers the entire area of the side of the nanotube forest. Given the measured current of 40 nA, laser power of 100 mW, and photon energy of 4.66 eV, this indicates a quantum efficiency of $\sim 10^{-5}$, which is two orders of magnitude higher than the value reported for MWNT matts [34] and approaches the quantum efficiency of metallic photocathodes currently employed (i.e. Cu has a quantum efficiency in the order of $\sim 10^{-5}$ for 266-nm light [17]). We speculate that this value may be further improved by optimizing the structural parameters of the nanotube forest such as nanotube length and inter-nanotube density. Photocathodes made from CNT forests would thus be promising for various applications, especially given that they are expected to be more robust and stable than conventional metallic surface photocathodes because of the nanotube's complete and strong chemical structure [25].

3.2.5 Optical Absorption in Nanotube Forests

To further understand the photoemission behaviour of CNT forests, we studied their optical properties using the effective optical constants of vertically aligned CNTs derived by García-Vidal *et al* [48] and solving the electromagnetic wave equation [49]. This problem can be modelled in three regions, as shown in Figure 3.4, where region one and three are free space and region two is the CNT forest. If we assume a plane wave, which is incident at $\theta = 90^\circ$ to the CNT forest (also shown in Figure 3.4), then the time-independent electric field in the first region can be written as $E_1 = E_{inc} + E_{ref}$, where E_{inc} and E_{ref} are the incident and reflected electric-fields at the boundary of the first and second region and have the following forms: $E_{inc} = \frac{\omega\mu_0}{k_1} \vec{z} \exp(-i\vec{k}_i \cdot \vec{r})$ and $E_{ref} = \frac{\omega\mu_0 H_r}{k_1} \vec{z} \exp(-i\vec{k}_r \cdot \vec{r})$. The time-independent magnetic-field in the first region can be written as $H_1 = H_{inc} + H_{ref}$, where $H_{inc} = \vec{x} \exp(-i\vec{k}_i \cdot \vec{r})$ and $H_{ref} = H_r \vec{x} \exp(-i\vec{k}_r \cdot \vec{r})$. The vectors \vec{k} and \vec{r} are the wave and position vectors and $|\vec{k}_i| = |\vec{k}_r| = k_1 = \frac{2\pi n_1}{\lambda}$. The amplitude of the incident magnetic field is assumed to be unity, ω is the light frequency, λ is the wavelength of light, and n_1 and μ_0 are the refractive index and permeability of free space. The electric and magnetic fields in the second region can be assumed to have the form of $E_2 = S_z(y) \vec{z} \exp(-i\vec{k}_{ix} x)$ and $H_2 = (\frac{\epsilon_0}{\mu_0})^{\frac{1}{2}} U_x(y) \vec{x} \exp(-i\vec{k}_{ix} x)$, respectively. It can be shown that $S_z(y) = a_2 \exp(i\alpha_2 y) + b_2 \exp(-i\alpha_2 y)$ and $U_x(y) = \frac{-1}{\omega(\mu_0 \epsilon_0)^{\frac{1}{2}}} \alpha_2 [a_2 \exp(i\alpha_2 y) - b_2 \exp(-i\alpha_2 y)]$ [49], where a_2 and b_2 are the amplitudes of left and right travelling waves in the second region, and $\alpha_2 = \sqrt{\omega^2 \mu_0 \epsilon_2 - k_1^2}$. The electric and magnetic fields in the third region are similar in form as the second

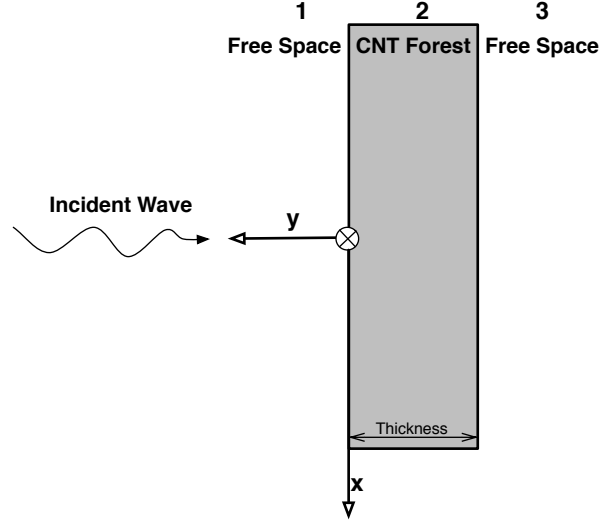


Figure 3.4: The direction of electromagnetic wave propagation is along the y-axis and the z axis is illustrated by \times .

except that there is no left traveling component. In order to compute the magnitude of the Poynting vector, we need to calculate the amplitude of the waves in the second region, namely a_2 and b_2 . This can be accomplished by equating the tangential components of the electric and magnetic fields at each region boundary, which will give the following:

$$\begin{bmatrix} -1 & \frac{k_1}{\omega\mu_0} & \frac{k_1}{\omega\mu_0} & 0 \\ 1 & \frac{-\alpha_2}{\omega\mu_0} & \frac{\alpha_2}{\omega\mu_0} & 0 \\ 0 & \exp(i\alpha_2 y) & \exp(-i\alpha_2 y) & -\exp(i\alpha_2 y) \\ 0 & \alpha_2 \exp(i\alpha_2 y) & -\alpha_2 \exp(-i\alpha_2 y) & -\alpha_3 \exp(i\alpha_3 y) \end{bmatrix} \begin{bmatrix} H_r \\ a_2 \\ b_2 \\ a_3 \end{bmatrix} = \begin{bmatrix} 1 \\ 1 \\ 0 \\ 0 \end{bmatrix}$$

This can be solved numerically. The flowchart for calculating the magnitude of the Poynting vector for different thicknesses of CNT forests is shown in Figure 3.5.

Figure. 3.6 illustrates the magnitude of the Poynting vector inside the nanotube forest for transverse-electric, 266-nm-light incident at $\theta = 90^\circ$ on a 1- μm -thick CNT forest. The simulations were done for two cases of polarization: electric field of the laser parallel (s-polarized) and perpendicular (p-polarized) to the axis of the nanotube. It is evident that s-polarized light does not penetrate the CNT forest by much and, within the first 10 nm, the magnitude of the Poynting vector is reduced by an order of magnitude; almost all the light is absorbed within the first few tens

3.2. Results and Discussion

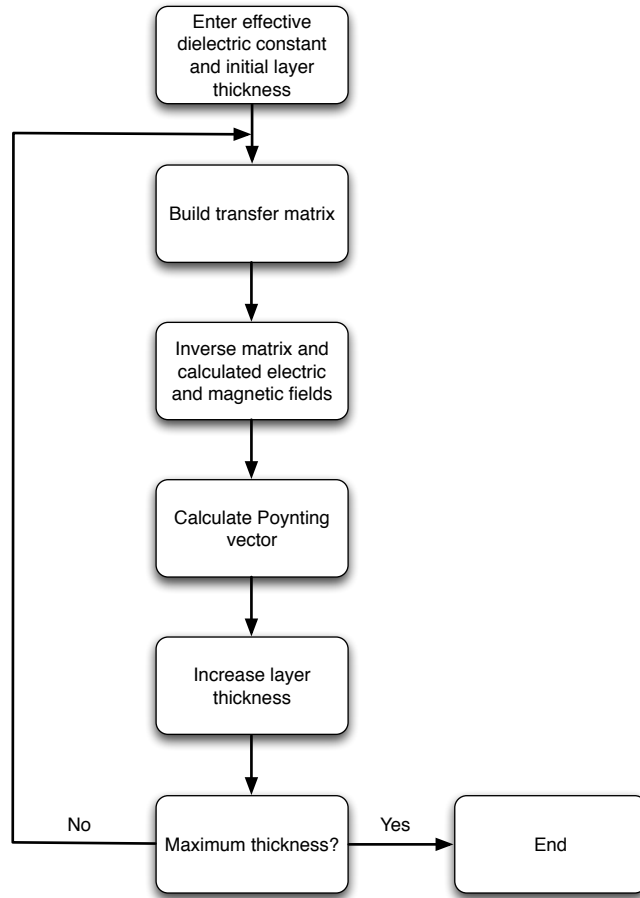


Figure 3.5: Flowchart for calculating the magnitude of the Poynting vector of the incident electromagnetic wave.

3.3. Summary

of nanometers. On the other hand, p-polarized light is hardly absorbed even within the first micrometer. In our experiments, the UV laser was circularly polarized and we expect its absorption behaviour to be somewhere between that of s- and p-polarized cases. Also, we recognize that these simulations only predict optical absorption and do not include the photo-electron emission process. Nonetheless, it is clear that a significant portion of the light does not penetrate deeper than a few tens of nanometers from the side of the forest, and whatever electron emission happens must happen from within that region. Also only the electrons that are generated near the surface of this layer are likely to escape the CNT forest since electrons that are generated deep in the layer are likely to get re-absorbed. Electron emission from this thin layer can potentially imply high emission current density.

The calculated reflectance for these forests is $\sim 10^{-3}$, which is consistent with the observation of Yang *et al.* [50] and Mizuno *et al.* [51] who have reported that CNT forests are an extremely dark material.

As a side note, given the significant difference in the decay lengths of the s- and p-polarized lights, it seems that a CNT forest could be used as an excellent polarizer, as demonstrated by Murakami *et al.* [52]. In this work we did not test the effect of s- and p-polarization since a polarizer was not available. These forests can also be shape engineered [53] to have sharp features to potentially improve their performance. They can also be grown on metallic contacts, which could then be easily integrated into accelerators and other electron-beam devices.

3.3 Summary

We demonstrated UV photo-electron emission from millimetre-long MWNT forests with quantum efficiencies in the order of $\sim 10^{-5}$ at low fields (pure photoemission) and $\sim 10^{-3}$ at an applied field of $0.3 \text{ V}\mu\text{m}^{-1}$. This is four orders of magnitude higher than the value reported for a matt of horizontal, randomly distributed MWNTs. Our simulations showed that the majority of the light is absorbed within the first few layers of the forest edge.

3.3. Summary

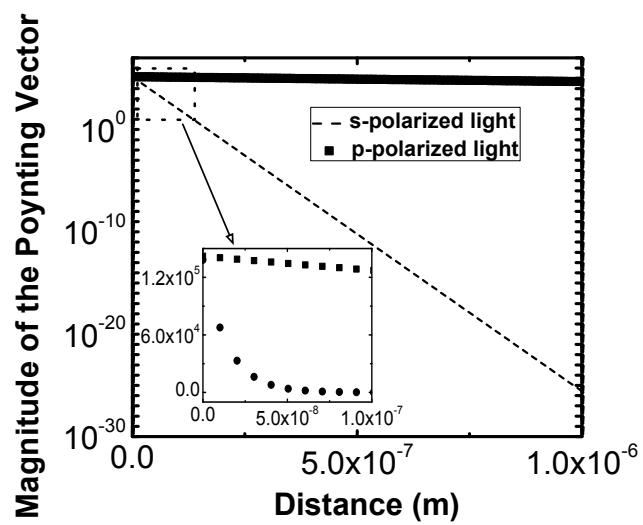


Figure 3.6: The magnitude of the Poynting vector as it travels through a 1-micrometer-thick CNT forest (logarithmic scale). Inset: non logarithmic plot of the first 100 nm. Notice the stronger absorption of s-polarized light.

Chapter 4

Visible-Light Induced Electron Emission from Carbon Nanotube Forests

4.1 Methodology

Chips with CNT forests were mounted on a specially made sample holder and placed in a high vacuum chamber ($\sim 10^{-7}$ Torr). The CNT forests were used as the cathode and a copper sheet was used as the anode, placed approximated 1 mm above the top surface of the CNT forests. The current was measured through the cathode. Laser light was brought into the chamber through a 200- μm -diameter optical fiber and collimated on the sidewall of the forest (Figure 4.1). The collimated beam covered an area of approximately 1 mm² of the side of the CNT forest. A Coherent Verdi V-5 laser ($\lambda = 532$ nm) and the main mode of an argon ion laser ($\lambda = 488$ nm) from a Spectra-Physics Beamlok 2060-10S equipped with electronics to stabilize the cavity for single mode operation (Z-lock and J-lock) were used as laser sources. A Keithley 6517A source/electrometer was used to apply voltage and measure the current.

4.2 Results and Discussion

The current-voltage characteristics of the CNT forest at different laser powers are illustrated in Figure 4.2. It is apparent that field-emission becomes dominant above 200 V (corresponding to an electric field of 0.2 V μm^{-1}) and saturates at about 300 V at all power levels. There are three distinct regions (as labelled on Figure 4.2). In region I, laser power has a drastic effect on the emission current. In region II, both

A version of this chapter has been published in Journal of Vacuum Science & Technology B. [54]

4.2. Results and Discussion

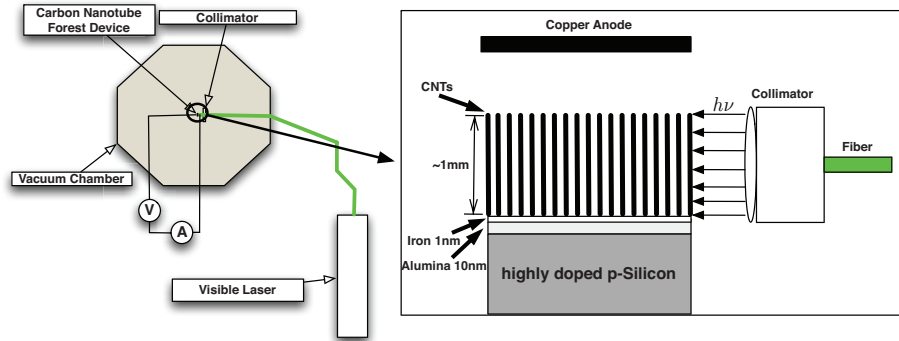


Figure 4.1: Schematic (not to scale) of the experimental configuration. The nanotube forest was grown on 1 nm of iron deposited on 10 nm of alumina. The laser irradiated the sidewall of the forest.

the applied field and the laser play a role, and a transition takes place where the relative effect of the laser decreases as the strength of the applied field increases. In region III, the laser has little effect on the electron emission and field-emission seems to be the only significant emission mechanism. Our interest in this work thus lies in regions I and II, which will be discussed in detail in the remainder of this section.

4.2.1 Region I

There are three mechanisms that could explain electron emission due to laser irradiation at low electric fields (region I of Figure 4.2), namely photo-mission, optical field-emission, and thermionic emission. Simple photo-emission cannot be the case since the photon energies involved (2.3 eV and 2.54 eV) are not high enough to enable the electrons to overcome the nanotube workfunction barrier (4.5-5.5 eV). Also, for photo-emission one expects a linear increase of current as a function of laser power, as previously demonstrated in chapter 3. Figure 4.3 illustrates the emission current as a function of power at the wavelength of 532 nm. The emission current grows non-linearly as a function of power. By the same argument, two photon-photo-emission is also likely not the cause of the emission current behaviour in region I Figure 4.2.

As discussed in section 1.2.3, in order to fit the experimental data to optical field-emission, we have to consider the effective DC electric field of the laser due to its intensity. This can be estimated by approximating the laser's electromagnetic

4.2. Results and Discussion

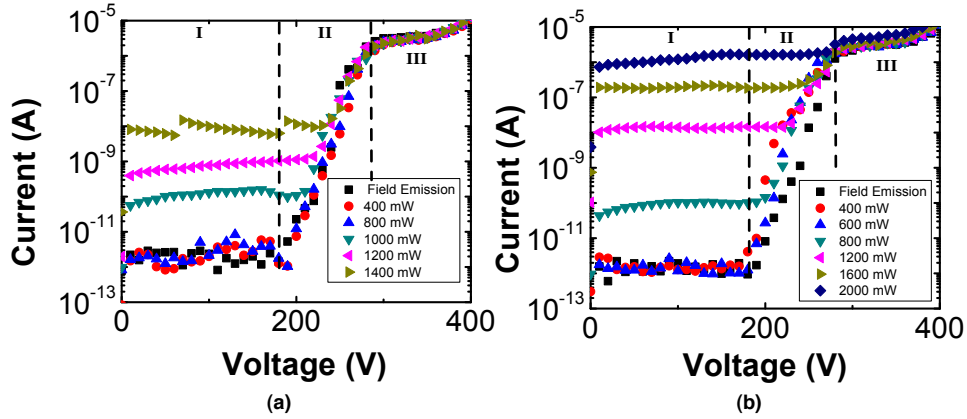


Figure 4.2: Emission current-voltage characteristics of the nanotube forest under different powers of: (a) 488-nm laser (the kinks on the 1400 mW curve are due to the stabilization electronics of the high power single mode operation of the argon laser) and (b) 532-nm laser. There are three distinct regions in the current-voltage characteristics.

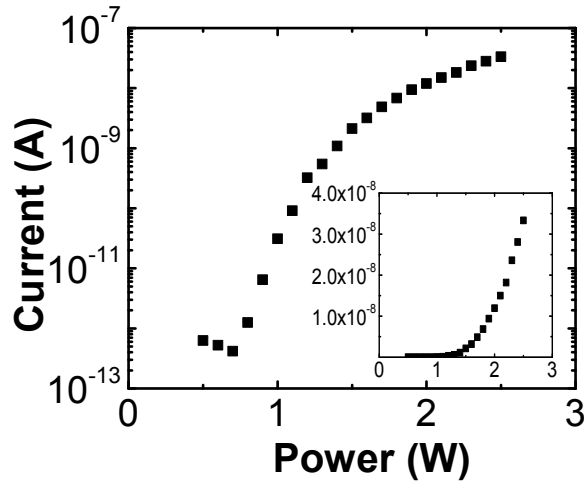


Figure 4.3: Emission current as a function of the incident optical power for illumination by the 532-nm laser. Only 1 V of bias was applied for collection of electrons and there was no field-emission in this case. Inset shows the curve on linear scale.

4.2. Results and Discussion

wave as a plane wave. The magnitude of the plane wave's time averaged Poynting vector is $\langle S \rangle = \frac{\epsilon_0 c}{2} E_0^2$, where ϵ_0 is the permittivity of free space, c is the speed of light and E_0 is the electric field amplitude. Given the ~ 1 mm diameter of the laser beam spot that is irradiating the CNT forest, the effective electric-field will be $\sim 0.01 \text{ V}\mu\text{m}^{-1}$ for a power level of 1 Watt. This field is about two orders of magnitude smaller than the needed field for field-electron emission from CNTs (which is $\sim 1 \text{ V}\mu\text{m}^{-1}$ before taking into account the field enhancement by the CNTs). Also, one would expect lower field enhancement at high optical frequencies unless the photon energy is close to a resonant state of the nanotubes such as the surface plasmon states. This is not the case here because nanotube plasmon states have energies greater than 5 eV [55, 56].

Thermionic emission maybe modelled by Richardson's equation and was discussed in section 1.2.2. In order to examine whether thermionic emission can explain the observed behaviour in region I, we need to estimate the temperature of the forest due to laser heating. This can be done by writing the power equilibrium equation for the system. The laser power input should dissipate in the system through emission of electrons and black body radiation. This can be expressed as [30]:

$$P_{Laser} = (\Phi + 2kT)A_G A T^2 e^{\frac{-\Phi}{kT}} + A\epsilon\sigma T^4 \quad (4.1)$$

, where A is the area of the laser spot, σ is the Stefan-Boltzmann constant and ϵ is the emissivity of the material (which is close to 1 for dark materials like CNTs). The first term on the right hand side of the equation is the power dissipated due to emission of electrons through a thermionic process (Richardson's law) and the second term is the power dissipated through black body radiation (Stefan-Boltzmann law). For simplicity, we have ignored the heat transfer to the substrate since we do not have much information on the heat conduction at the CNT forest and substrate junction and no heating of the substrate was observed. This assumption has previously been observed to be accepted in a similar situation [30].

By using this expression the temperature of the CNTs due to laser heating was calculated and then used in Richardson's equation, which shows a reasonable fit to our experimental data (Figure 4.4). The parameters that were used for this fit are $\epsilon = 1$, $\Phi = 4.6\text{eV}$, and a spot radius of $\sim 500\mu\text{m}$. The ratio between power dissipated by emitted electrons (the first term of equation 4.2.1) to power dissipated by radiation (the second term of equation 4.2.1) increases exponentially

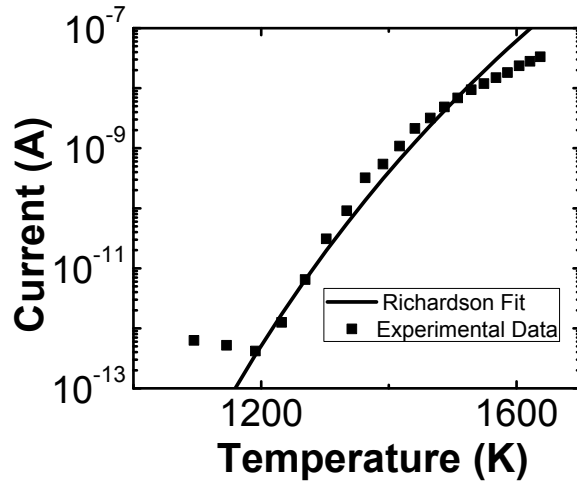


Figure 4.4: Emission current as a function of the calculated temperature by the 532-nm laser. Only 1 V of bias was applied for collection of electrons and there was no field-emission in this case. The solid line shows the Richardson fit to the data.

as a function of temperature. For example, at 1200 K this ratio is $\sim 10^{-13}$ and by 1600 K this ratio increases to $\sim 10^{-7}$.

Note that in these experiments, we had no visual contact with the device inside the vacuum chamber in order to observe an incandescent glow as a result of the high temperature. In subsequent, related experiments, we have indeed observed such a glow, and the corresponding optical spectra indicate temperatures in the range of 1,000-2,000 K. The details of those experiments are described in chapter 5.

At high temperatures, the fit diverges from the data, which maybe because our power measurements were done before the laser beam was coupled into the fiber. The beam waist of the laser increases (by a small amount) with increasing power, which is typically due to imperfections of the laser's cavity. This increase in waist size can reduce the amount of coupling between the laser and the fiber at high powers and since we are calculating the temperature from the measured power, then the temperature and correspondingly the emission current would be over estimated in this region. For example, if the laser-fiber coupling reduces the output power of the fiber by 5% at the high power regime, then the temperature could be reduced by as much as 100 K, which corresponds to an order of magnitude change in emission current.

4.2.2 Region II

In region II of the current-voltage characteristics, both the applied field and the laser have an effect, and the relative effect of the laser decreases as the field increases. In this region, photo-field emission, that is the excitation of electrons to higher energy levels as a result of absorption of photons and their subsequent tunnelling through the vacuum barrier (as described in section 1.2.3), could play an important role. To understand this laser-assisted field-emission region better, we plot the data of Figure 4.2(a) and (b) on the so-called Fowler-Nordheim (FN) scales [11, 57] on Figure 4.5. In region II, we can see two distinct slopes (slope I and slope II) on the (no laser) field-emission curve (it should be noted that multiple linear regions on FN curves have been observed in CNT field emitters before [58]). However, on the curves with different laser powers there is a distinct third slope (slope III), which differs from the field-emission slope at similar fields. The ratio of slopes on FN axes is equal to the ratio of the effective work functions corresponding to the curves to the power of one-half. This can be shown by taking the logarithm of both sides of equation 1.2, which will give a linear equation with a slope of $\frac{H\Phi^{1.5}}{\beta}$. Taking the ratio of two slopes corresponding to two different effective workfunctions (i.e. Φ_1 and Φ_2) will give $\frac{(\Phi_1)^{1.5}}{(\Phi_2)^{1.5}}$, assuming that the enhancement factor (β) remains the same for both curves, which is a reasonable assumption for this experiment.

In the case of the 532-nm laser (Figure 4.5(a)), the ratio of slope I to slope III is ~ 2.9 . This value is very close to the ratio of the work function of a CNT (~ 4.6 eV) divided by the reduced work function of a CNT by photons with energy of 2.3 eV ($\lambda = 532$ nm) to the power of one-half (i.e. $\frac{(\Phi_{CNT})^{1.5}}{(\Phi_{CNT-E_{Photon}})^{1.5}} = \frac{(4.6)^{1.5}}{(2.3)^{1.5}} \approx 2.8$). It appears that when the electric field is high enough and the laser power is too low for thermionic emission (i.e. region II of the current-voltage curve at low laser power), photo-field emission can play an important role. If the optical power is further increased (the curves corresponding to 1,600 mW and 2,000 mW for the 532-nm laser), the relative effect of the field becomes less pronounced and it becomes more difficult to observe this photo-field emission effect in the transition region II. Adsorbates also have an effect on the workfunction of a material and their desorption as a result of laser heating could alter the effective workfunction, thus affecting the emission current. However, their effect is usually less than 1 eV in terms of workfunction change [59]. Nonetheless, we cannot rule out the possibility that adsorbates could play an important role in this emission regime, despite the high vacuum level of $\sim 10^{-7}$ Torr used in the experiments. Temperature dependence of field-emission could also play a role in this region; however, in this case

4.3. Summary

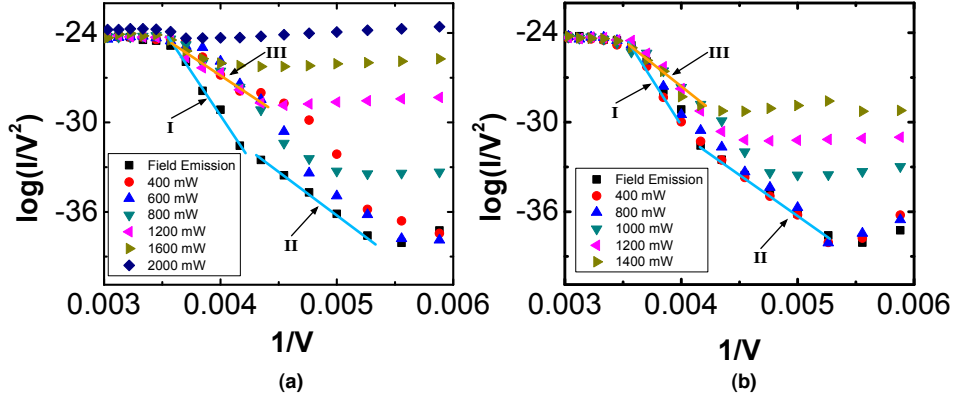


Figure 4.5: Fowler-Nordheim plot corresponding to the data of Figure 4.2(a) and (b). Indicated are two different slopes on the (no laser) field-emission curve (slope I and II) and a third slope (slope III) on the low-laser-power curve at high fields. The ratio of slopes I and III for (a) is ~ 2.9 and for (b) is ~ 2.3

one would expect the slope of the curves corresponding to different laser powers to differ from one another as each curve also corresponds to a different temperature. This is obviously not the case here.

Light activated electron sources can have applications ranging from radio frequency cathodes used in accelerators and free-electron lasers to modern solar cells [5]. In this work, we have demonstrated thermionic electron emission from CNT forests with a light intensity that is several orders of magnitude smaller than previously reported for pure CNTs [34]. This low-light-power activated electron source can not only improve the performance of electron sources in existing applications, it can also enable new applications in micro vacuum technology, such as on-chip electron sources activated using integrated lasers.

4.3 Summary

Millimeter-long vertical MWNTs were irradiated with CW visible lasers with wavelengths of 532 nm and 488 nm. Three distinct regions of electron emission were identified. In the first region (at low electric fields), laser irradiation has a strong effect on the emission current, with strongly non-linear increase in current as a function of laser power with an on/off ratio of 10^6 . The mechanism responsible for this behavior was identified as being primarily laser induced thermionic emis-

4.3. Summary

sion. The second region of the current-voltage characteristics only shows a minor dependance on laser power and, at high electric fields in this region, photo-field emission seems to be playing a role. The third region seems to be dominated by field-emission since all the curves saturate to almost the same level. The first two regions of emission due to laser can have applications in vacuum electronics and electron beam lithography and machining.

Chapter 5

A “Heat Trap”

Light-Induced Thermionic Electron Source Using Carbon Nanotube Arrays

5.1 Introduction

To better understand the non-linear behavior of electron-emission as a function of optical-power, a different experiment was carried out whereby the CNT sample was placed right next to a viewport and the laser was focused onto the sample with a lens. This enabled us to have visual contact with the heated region and carry out further analysis, which is presented in this chapter.

5.2 Methodology

The experiments were performed in a high vacuum chamber with a pressure of $\sim 10^{-8}$ Torr. A copper anode was placed approximately 1 mm away from the top surface of the nanotube forest. The anode was larger than the forest in order to provide good electron collection efficiency from all sides of the forest. The entire device (including both cathode and anode) was placed on a micrometer stage with a movement resolution of $0.5 \mu\text{m}$ in the vacuum chamber. This allowed us to move the sample accurately in and out of the focal point of the laser as needed in the experiments where a gradual change of the intensity was needed. A Keithley 6517A electrometer served to apply the collection voltage and measure the emission current at the cathode. Figure 5.1 shows the schematic diagram of the experimental

A version of this chapter has been published in Solid State Communications. [60]

5.2. Methodology

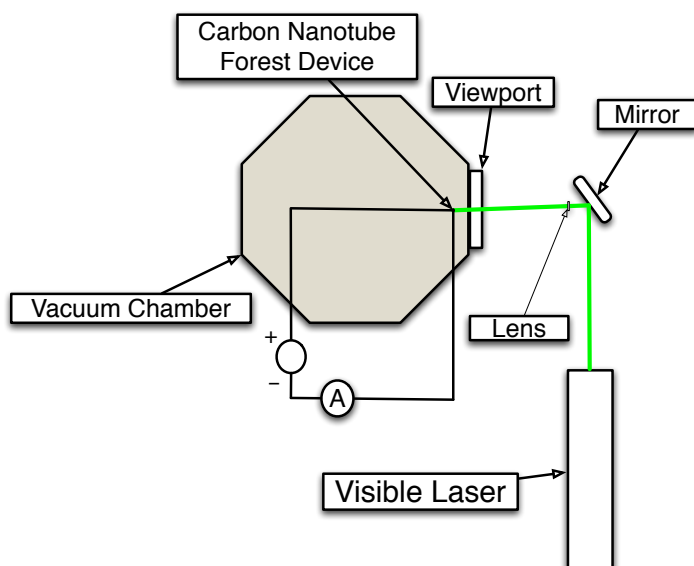


Figure 5.1: Schematic of the experimental apparatus where the laser is focused with a lens, placed outside of the vacuum chamber, on the sidewall of the nanotube forest through a sapphire viewport.

configuration. A laser beam was focused onto a spot with a diameter in the range of 50-250 μm on the side of the nanotube forest (Figure 5.2) through a sapphire viewport with a transparency of $> 80\%$ in the visible range. We used a Coherent Verdi-5 solid-state laser to obtain the 532 nm line and a Spectra-Physics Beamlok 2060-10S argon ion laser to obtain the 514 nm and 488 nm lines. Both provided continuous-wave beams. If a cathode-anode voltage of more than 150 V was applied, field-emission would happen from the nanotube forest. For voltages below this value (which is the case discussed here), there was no field-emission and the emission current was only due to laser illumination. The optical spectra of the incandescent spot was measured by focusing its image onto an optical fiber connected to an Ando AQ-6315A optical spectrum analyzer. The spectra were corrected for the response of the fiber and a least-squares method was used to fit the black body curves to the experimental data and find the temperature in each case.

5.3 Results and Discussion

5.3.1 Light-Induced Thermionic Emission with Low Power Laser

One way to heat a material locally is by illuminating it with a beam of light. Although this can be achieved easily for a spot on an insulating surface, it requires significantly higher optical power for a similar spot on a metallic surface, due to efficient dissipation of heat to the surroundings. We found in a continuous-wave visible laser beam with a diameter as small as $\sim 100 \mu\text{m}$ results in a heated, incandescent spot with approximately the same size on the nanotube forest. We obtained an emission current of 100 nA for an optical power as low as 4 mW from a small handheld laser. The emission current showed a strong nonlinear increase with laser power and reached 25 μA at 350 mW.

Forests of vertically aligned carbon nanotubes are excellent absorbers of light over a wide spectral range, similar to a perfect black body [1, 2]. Laser-induced heating of nanotube films [61] and thermionic electron emission from nanotube forests [47] have been reported. On the other hand, the high or moderate thermal conductivity of nanotubes [62, 63, 64, 65, 66, 67] has motivated applications in thermal management [68]. In the above experiments, therefore, high-power pulsed lasers or a beam wide enough to heat the entire nanotube sample were needed, as one expects that any heat generated locally in one section of a nanotube would efficiently dissipate by conduction through the rest of it and not lead to a major increase in temperature, such as observed in optical absorption and thermal transport experiments on suspended nanotube bundles [69].

Here, we show that the situation is different if the light intensity is beyond a certain threshold, even for low total optical power. Figures 5.1 and 5.2 show a schematic of the device and experimental configuration. The photon energies of 2.33-2.54 eV used (wavelengths of 488-532 nm) are well below the workfunction of carbon nanotubes (4-5 eV [70, 71]) for pure photo-emission (photoelectric effect) to happen; no current is expected if the collection voltage at the anode is not high enough for field-emission. Indeed, that was the case if the laser beam was not focused enough. Remarkably, however, as we focused the beam to smaller spots (increasing the intensity at fixed power), we observed a drastic change in behaviour: a bright, localized incandescent glow appeared suddenly on the forest sidewall at the location of the laser spot (Figure 5.2(b)) and an emission current appeared. For example, at 100 mW of laser power focused to a 0.2 mm^2 area (corresponding

5.3. Results and Discussion

to an intensity of 0.5 Wmm^{-2}), we measured an emission current of $\sim 100 \text{ pA}$.

Figure 5.3 shows the emission current as a function of laser power when the laser is focused beyond the threshold intensity. The observed non-linear increase is consistent with thermionic emission. Figure 5.4 shows the measured current as a function of device temperature (obtained by fitting the optical spectrum of the glow spot to that of black body radiation - Figure 5.5), as well as the calculated current using the Richardson-Dushman equation for thermionic emission, following the trend of the experimental data. Another possible mechanism would be optical field-emission (field-emission as a result of the modulation of the vacuum barrier by the electric field of the laser) [72]; however, even at the maximum intensity used here, the electric field of the laser beam was only $\sim 0.1 \text{ V}\mu\text{m}^{-1}$, significantly below the required field of $\sim 1 \text{ V}\mu\text{m}^{-1}$ for field-emission from carbon nanotubes. Effects such as two-photon photo-emission or a combination of photo- and thermionic emission [73] may also play a role, although the dominant mechanism seems to be thermionic.

When slowly moving the sample out of the focal point, we first noticed a gradual decrease in the emission current, indicating that widening the beam and reducing the intensity leads to a lower temperature at the emission spot. At a threshold intensity, however, the current dropped suddenly and the visible glow disappeared.

5.3.2 “Heat Trap” Mechanism

The extreme localization of heat observed here (incandescent spot size approximately the same as laser spot size) is highly unusual and, given the relatively high thermal conductivity of nanotubes, very counterintuitive. We explain the phenomenon as follows. We believe the key lies in the fact that thermal conductivity drops as a function of temperature at high temperatures (indeed, a $\frac{1}{\alpha T + \beta T^2}$ behaviour for thermal conductivity has been reported for temperatures up to 800 K in individual single-walled carbon nanotubes [74, 75, 76], which is attributed to umklapp and second-order three-phonon scattering [74, 77, 78]), and the anisotropic nature of the nanotube forest. As the laser intensity increases, the rate of heat generation in the nanotube forest increases. Below the threshold, this heat can dissipate along the nanotubes’ axis and the temperature slowly rises by a small amount, as in Ref. 74. Above the threshold, however, the rate of heat generation is significantly higher than that of dissipation, such that the temperature at the laser spot rises quickly, reducing thermal conductivity in that region, which then leads to even more effective heating of that spot. The resulting positive feedback mech-

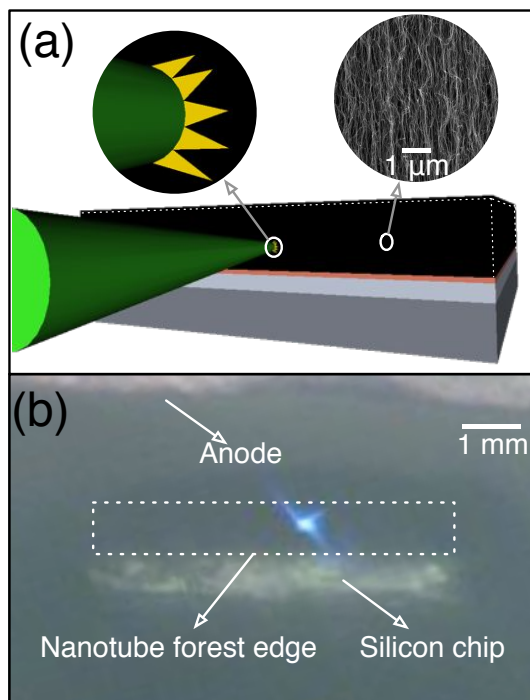


Figure 5.2: (a) Schematic of the device showing the laser spot on the sidewall of the carbon nanotube forest. An incandescent spot is observed as the intensity of the laser is increased. The top left inset demonstrates that the incandescent spot is localized to the position of the laser beam and does not spread as the laser intensity is increased. The top right inset shows a scanning electron micrograph of the sidewall of an actual carbon nanotube forest and the nanotubes' overall alignment. (b) The photo of the device with the incandescent spot. The laser light has been filtered out and the glow has been attenuated in order to image the spot using a CCD camera. The white dotted box is used to draw attention to the sidewall of the forest. The silicon chip, on which the nanotubes are grown, and the edge of the copper anode, which collects the emitted electrons, are also shown.

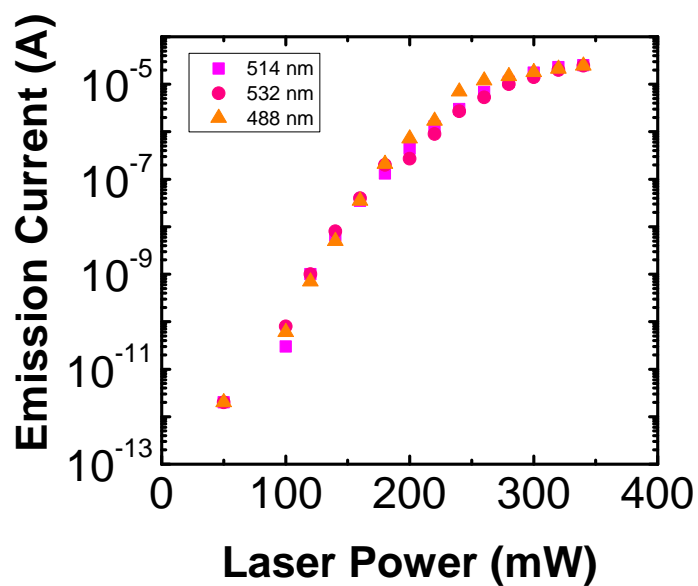


Figure 5.3: The measured emission current versus the laser power for several wavelengths (488 nm, 514 nm, and 532 nm) shows a non-linear increase. The behavior is very similar in all cases, consistent with broad spectral absorption of CNTs [1, 2]. The laser spot was $\sim 250 \mu\text{m}$ in radius. A collection voltage of 50 V was applied, which is below that needed for field-emission (dark current is below the measurement noise). There is a threshold (or turn-on) region where the intensity of the laser is high enough to cause localized temperature increase and electron emission.

5.3. Results and Discussion

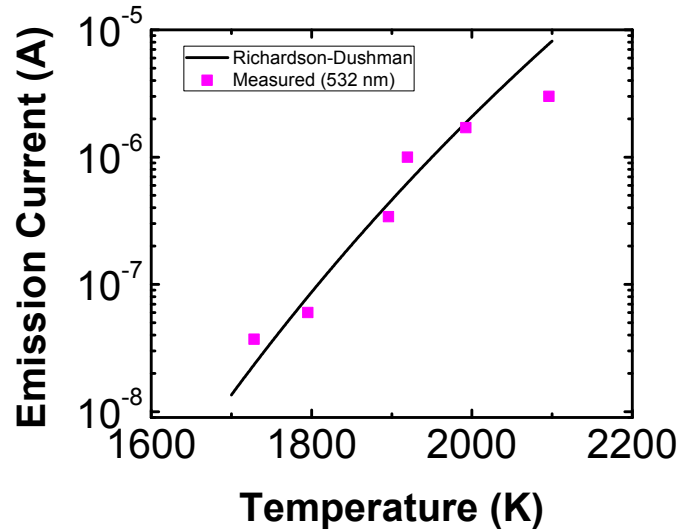


Figure 5.4: The measured emission current as a function of emission spot temperature (at 532 nm) shows a trend similar to that predicted by the Richardson-Dushman equation. The laser spot had a radius of $\sim 250 \mu\text{m}$. The dotted curve shows the current as a function of the measured temperature, which was determined by fitting the black body spectrum to the spectrum of the incandescent spot. The solid line shows the prediction of the Richardson-Dushman equation, where an emission spot radius of $\sim 230 \mu\text{m}$ was chosen to obtain this fit. The error bars for the measured emission current are much smaller than the graph markers and therefore not seen.

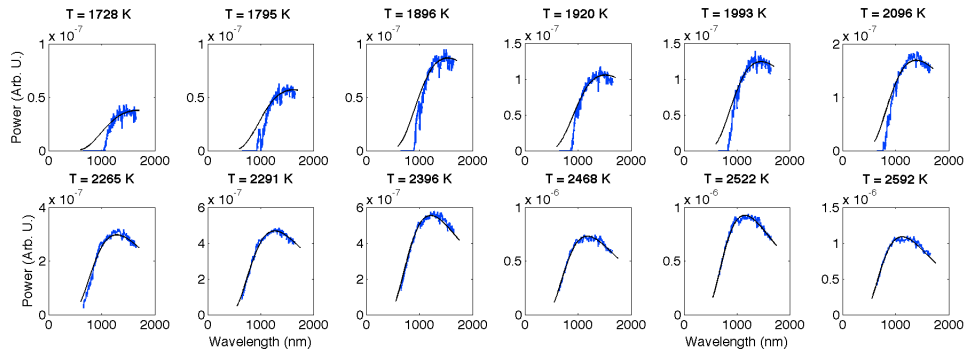


Figure 5.5: Optical spectra of the incandescent spot. The blue lines are the measured spectra, corrected for the response of the coupling fiber, and the black lines are Planck's black body radiation fits. The corresponding temperatures is shown above each graph.

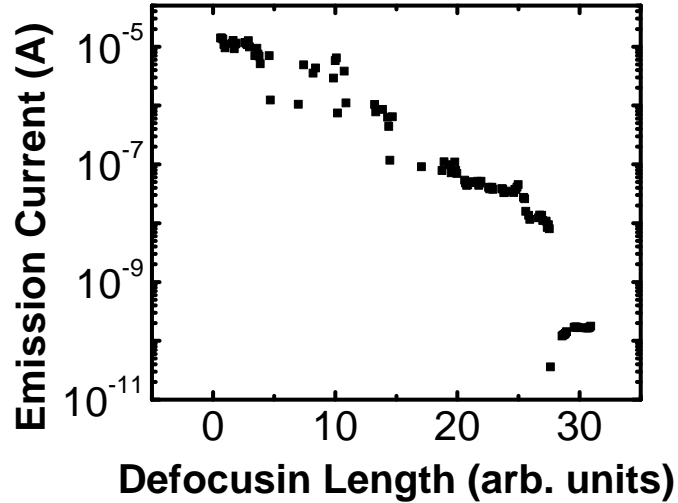


Figure 5.6: Measured emission current as the laser beam is defocused by moving the CNT sample along the axis of the laser beam. The emitted current slowly decreases as the laser spot becomes larger and then the CNT sample suddenly stops emitting electrons. This sudden stop of emission is the threshold of “Heat Trap” where the heat induced by the laser can now easily dissipate along the CNT as its thermal conductivity increases with reduced temperature.

anism leads to a significant increase in the temperature and corresponding drop of thermal conductivity in that region, thermally isolating it from the surrounding area and allowing efficient heating to high temperatures. Such a heat localization has not been observed in bulk conductors. The threshold becomes very apparent as we slowly defocus the laser spot on the sidewall of the CNT forest. Figure 5.6 demonstrates this effect by showing a slow decrease in emission and then a sudden turn-off point as the beam is further defocused.

5.3.3 Modelling of the “Heat Trap” Mechanism

This behaviour can be added to equation 4.2.1 by adding a heat dissipation term (shown in equation 5.1). We did not have to include the energy dissipated due to thermal conductance of nanotubes in the previous chapter since the entire side of the CNT forrest was heated and no heating of the substrate was observed.

5.3. Results and Discussion

$$P_{Laser} = (\Phi + 2kT)A_GAT^2e^{\frac{-\Phi}{kT}} + A\epsilon\sigma T^4 + k(T)(T - T_{room})\frac{A_{heat}}{L} \quad (5.1)$$

The constants in the first two terms on the right handside of the above equation are the same as in equation 4.2.1. T_{room} is the room temperature and A_{heat} is the cross-sectional area of the hot spot in the direction perpendicular to the nanotubes (spot diameter times depth) as shown in Figure 5.7. The localized heated area (the orange spot shown in Figure 5.7(a)) will only affect a small number of nanotubes (Figure 5.7(b)) because the thermal conductivity between neighbouring nanotubes is low [63], which will also limit how deep the heat can penetrate the nanotube forest to how far the light can penetrate the forest. This rectangular area (shown in Figure 5.7(c)) is A_{heat} , which is multiplied by the concentration of nanotubes in the forest ($\sim 10\%$) since only a small portion of the rectangle is occupied by nanotubes (shown in Figure 5.7(d)). The depth of this rectangle is estimated using the optical simulation discussed in section 3.2.5. L is the distance between the hot area (where electron emission occurs) and the room-temperature area, which is where the nanotubes are not glowing. $k(T)$ is the temperature dependent thermal conductivity of the nanotube forest along the tubes' axis, which we took to be $\frac{1}{\alpha T + \beta T^2}$. This behaviour has been observed for individual nanotubes up to a temperature of approximately 800 K with values of 3.7×10^{-7} and 9.7×10^{-10} for α and β , respectively [74, 75, 76]. Here, we assumed that this behaviour applies to the nanotube forest as well, and continues in the temperature range of our data. For simplicity, we assumed the temperature to be constant across the entire spot (area A) and then decay linearly to the rest of the nanotube forest over the length L described before. Although these assumptions may be simplistic, our goal here is not the accurate, quantitative prediction of the temperature, since the temperature has already been measured using spectroscopy as discussed before. Instead, we are interested to investigate whether a $\frac{1}{\alpha T + \beta T^2}$ behaviour for thermal conductivity and the anisotropic nature of heat dissipation can provide a reasonable fit to the experimental data, in order to further support our explanation of the physical mechanism responsible for the observed phenomenon.

Figure 5.8 shows the difference between temperature as a function of laser intensity in an anisotropic material (Figure 5.8(a)) and an isotropic material (Figure 5.8(b)) for different laser spot areas. The thermal conductivity in the isotropic material is assumed to have a $\frac{1}{T}$ behaviour, which is a well accepted behaviour for bulk materials. The curve for an anisotropic material changes as a function of

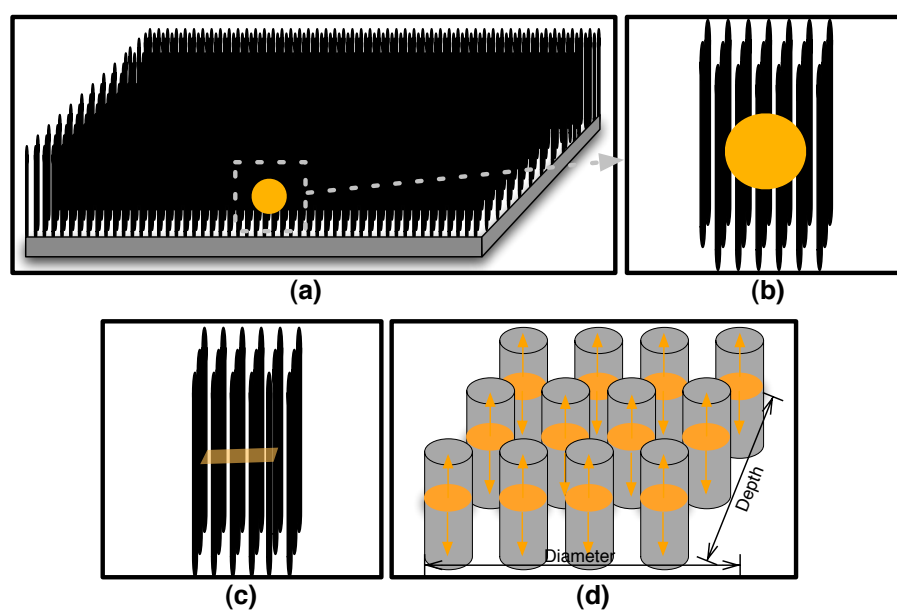


Figure 5.7: (a) Drawing of the localized heated area on the nanotube forest. (b) Zoomed-in drawing of the heated area. (c) Drawing of the the cross section of the heated spot. (d) Zoomed-in drawing of the heated spot with arrows showing the direction of heat dissipation.

5.3. Results and Discussion

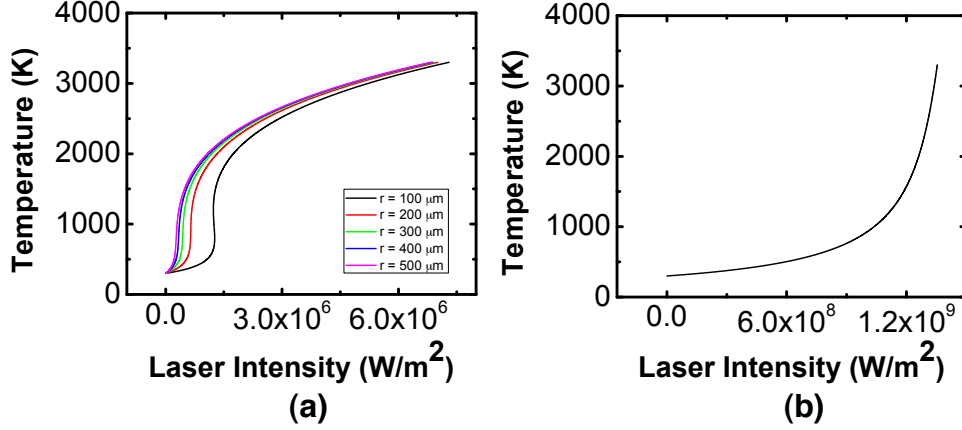


Figure 5.8: (a) Temperature as a function of laser intensity for an anisotropic material (i.e. nanotube forest) and a $\frac{1}{\alpha T + \beta T^2}$ thermal conductivity behaviour for different laser spot areas. (b) Temperature as a function of laser intensity for an isotropic material and a $\frac{1}{T}$ thermal conductivity behaviour. The curve remains the same for different laser spot areas (explained in text). The parameters used for this figure were: $\epsilon = 1$, $\Phi = 4.6$ eV, $L = 14$ μm , $T_{\text{room}} = 300$ K, and the depth for calculating A_{heat} of the anisotropic case was calculated to be ~ 50 nm. The input power has been corrected for the transparency of the sapphire viewport (85% at 532 nm).

laser spot size but the curve for an isotropic bulk material stays the same. This is because the ratio of area of heat dissipation to the spot size ($\frac{A_{\text{heat}}}{A}$) for different laser spots will change as a function of $\frac{1}{r}$ for the anisotropic material but it will stay the same for the isotropic material. This can be demonstrated by dividing equation 5.1 on both sides by the heated area (A), which we assume to be the same size as the laser spot area, to calculate laser intensity as a function of temperature. All A terms will disappear on the right side and only a $\frac{A_{\text{heat}}}{A}$ will remain in the thermal conduction term. For the anisotropic case, $A_{\text{heat}} = 2 \times \text{radius} \times \text{depth}$; therefore, $\frac{A_{\text{heat}}}{A} = \frac{2 \times \text{depth}}{r \times \pi}$ given $A = \pi \times r^2$. For the isotropic case, A_{heat} , the surface area of the sphere that the heat dissipates through ($A_{\text{heat}} = 4 \times \pi \times r^2$) and, therefore, $\frac{A_{\text{heat}}}{A} = 4$.

It is also important to note the difference in the rate at which the temperature increases in the two different cases shown in Figure 5.8. For the anisotropic case the temperature increases rapidly at a threshold intensity, which we have observed experimentally, but for the isotropic case the temperature increases more slowly.

5.3. Results and Discussion

The figure also shows a large difference (about three orders of magnitude) in laser intensity for increasing the temperature of the material to the thermionic emission region (~ 2000 K). Indeed as we heated a piece of tungsten (obtained from a light bulb) in order to observe 100 nA of current emission an intensity of three orders of magnitude higher than that for nanotube forests was needed, although reflectance from tungsten is only 50%. In addition, the size of the glowing region was ~ 100 times larger than the size of the laser spot, indicating high heat dissipation to the surrounding areas. The response of the tungsten wire was also very slow as the gradual heating was easily observed with the naked eye to take a few seconds, and a rise time of ~ 2 seconds was seen in the thermionic emission current. In the case of the nanotube forest, the response was instantaneous as seen by the naked eye and, as we chopped the laser beam with a frequency of up to 100 Hz, the emission current showed an alternating behaviour with the same frequency. All these observations point to the unique behaviour of the nanotube forest.

The threshold intensity at which point the temperature increases rapidly for the anisotropic case occurs when the derivative ($\frac{dI}{dT}$) of equation 5.1 equals to 0. $\frac{dI}{dT}$ can be derived to be:

$$\begin{aligned} \frac{dI}{dT} = & (\Phi + 2kT)(2A_G T + \frac{A_G \Phi}{k}) e^{\frac{-\Phi}{kT}} + 2A_G T^2 k e^{\frac{-\Phi}{kT}} + 4\epsilon\sigma T^3 + \\ & \frac{A_{heat}}{AL(\alpha T + \beta T^2)} + \frac{A_{heat}(T - T_{room})(\alpha + 2\beta T)}{AL(\alpha T + \beta T^2)^2} \end{aligned} \quad (5.2)$$

By setting the above equation to 0 and calculating the corresponding temperature, the threshold intensity can be calculated. This cannot be done analytically, but it can be done numerically. Figure 5.9 shows the threshold intensity as a function of the laser spot radius. The calculated threshold intensities shows a $\frac{1}{r}$ behaviour (dotted line).

5.3.4 Experimental Fit to the Proposed Model for “Heat Trap”

Figure 5.10 shows the emission current as a function of power. Both the measured values (corresponding to the data in Figure 5.4) and the values calculated by determining the temperature from the power equilibrium equation and using it in the Richardson-Dushman equation are plotted. The good fit obtained supports the suggested behaviour for the thermal conductivity of the nanotube forest in the wide range of temperatures discussed here. In order to obtain the above fit, the distance

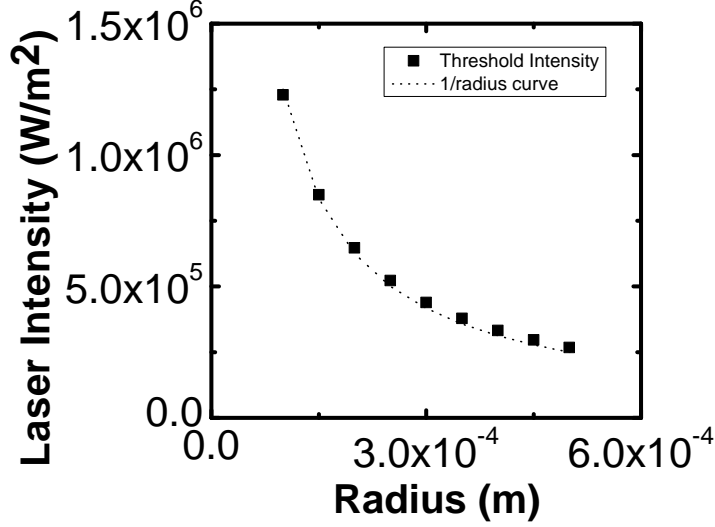


Figure 5.9: Laser intensity threshold as a function of laser spot radius. The illustrated behaviour follows a $\frac{1}{r}$ trend.

L was found to be $25.5 \mu\text{m}$, which seems quite reasonable. The resolution of our imaging system does not allow an accurate measurement of L . Also, note that in equation (5.1) the parameters $k(T)$, A_{heat} , and L all appear in one term and we cannot determine them independently. For instance, it is quite possible that, due to the wavy nature of the nanotubes in the forest and inter-nanotube coupling, the thermal conductivity of the forest is smaller than that of individual nanotubes, corresponding to larger values for α and β compared to those reported in Ref. 74. If we choose a larger α and β , we obtain a correspondingly smaller L . Therefore, we cannot determine the actual value of thermal conductivity, but rather confirm its $\frac{1}{\alpha T + \beta T^2}$ behaviour.

We note that defects could also reduce thermal conductivity [79]; however, defects cannot explain the abrupt turn-on we observe at the threshold intensity. Moreover, one expects defects to partially heal at the elevated temperatures attained here. However, we have not observed weakening of the phenomenon after repeating the experiment many times, which suggests defects do not play a major role here.

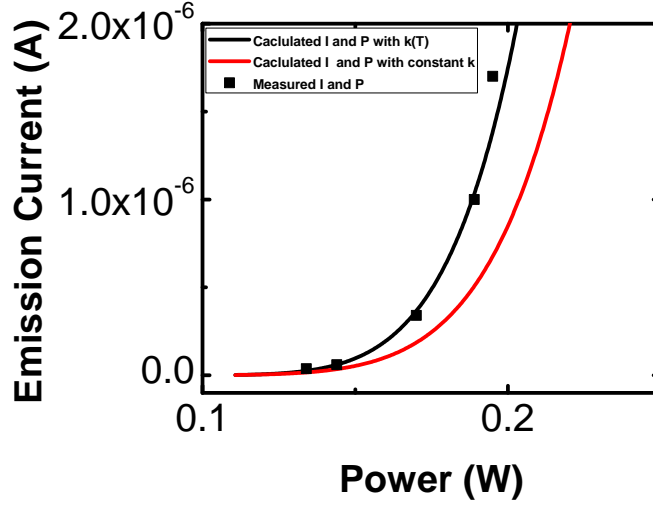


Figure 5.10: Emission current as a function of laser power. The calculated data have been obtained by finding the temperature using the power equilibrium equation and using it in the Richardson-Dushman equation for thermionic emission. The solid red line shows the calculated emission current with using a constant value for the thermal conductivity, which provides a good fit at low emission current but diverges at high emission. On the other hand, the solid black line, which uses a $\frac{1}{\alpha T + \beta T^2}$ behaviour for the thermal conductivity provides a good fit. The parameters used for this Figure are: $r = 240 \mu\text{m}$, $\epsilon = 1$, $\Phi = 4.6 \text{ eV}$, $L = 25.5 \mu\text{m}$, $T_{room} = 300 \text{ K}$, and the depth for calculating A_{heat} of the anisotropic case was calculated to be $\sim 50 \text{ nm}$. The input power has been corrected for the transparency of the sapphire viewport (85% at 532 nm).

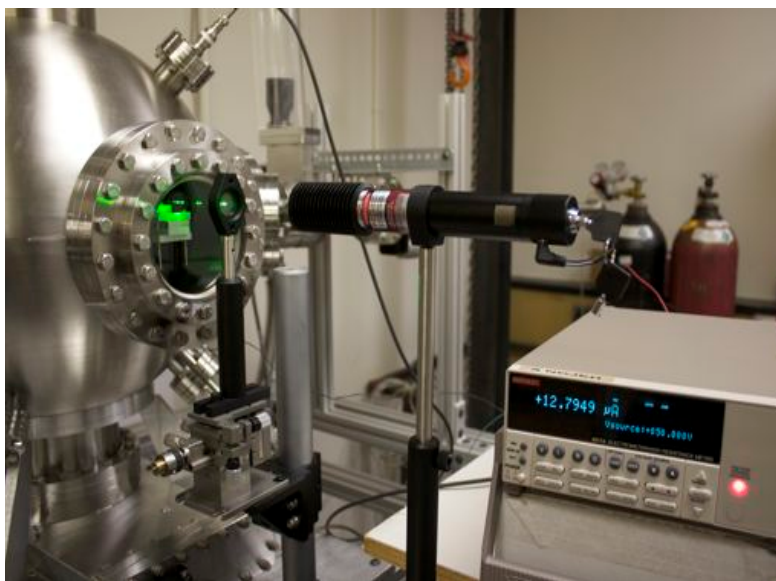


Figure 5.11: A 50 mW, battery-operated hand-held laser was capable of heating the sample enough for thermionic emission. The laser was focused onto the sidewall of the forest using a lens with a 15-cm focal length. The sample is inside of the high vacuum chamber seen on the left and placed close to the sapphire viewport. An emission current of $\sim 13 \mu\text{A}$ is recorded by the electrometer through an insulated BNC feedthrough by applying a collection voltage of 50 V. This experiment demonstrates that laser-activated thermionic cathodes do not have to rely exclusively on sophisticated high-power pulsed laser anymore - a laser pointer and potentially even integrated lasers may also work.

5.3.5 Applications

The observed efficient, localized heating at optical powers down to 4 mW is remarkable since it opens up the possibility of photon-to-electron conversion devices using readily available light sources such as laser pointers, lamps and even the sun. In Figure 5.11 we show a photograph of the experiment where an inexpensive hand-held laser was used at a power of 50 mW to generate $\sim 13 \mu\text{A}$ of emission current. This corresponds to a quantum efficiency (if we were to define one for thermionic emission) of 0.06%; however, this value can be increased if the laser is focused to a smaller spot to increase the intensity further.

We also repeated the experiment by focusing the laser on the top surface of

5.4. Summary

the nanotube, again obtaining a similar effect, in agreement with the fact that in Ref. 1 a low reflectance was observed for a wide range of illumination angles. The experiments were repeated numerous times over several months, while other experiments (such as ultra-violet photo-emission) were also performed on the same device in-between. The device showed remarkable robustness and the results were consistently reproducible. Three other nanotube forests, prepared with the second generation CVD reactor recipe, were also tested and they all exhibited the same effect in a reproducible manner at various locations on each forest. It is thus evident that the observed phenomenon is not a coincidence and has its origin in the fundamental structure and properties of the nanotube forest.

Finally, a note is in order on the effect of polarization of the incident light: the thermionic current was substantially higher (one to three orders of magnitude higher in experiments on various samples and different locations on each sample) for polarization parallel to the axis of the nanotubes, consistent with our previous optical absorption simulations, shown in section 3.2.5, where we observed significantly stronger optical absorption for parallel polarization.

5.4 Summary

Previously, electrically driven thermal light emission [80] and thermionic emission [81] have been demonstrated in nanotubes. Trapping of optically induced thermal energy in individual single-walled nanotube bundles has also been observed (not observed in multi-walled samples) [82]. Localized glow of nanotube forests under ultra-violet laser has been reported in Ref. 42. However, the glow spectrum in that case exhibited photoluminescence behaviour rather than black body radiation corresponding to high temperature. Here, we reported light-induced heating, incandescence and thermionic emission confined to an island on the side surface of a macroscopic-size multi-walled nanotube forest. Given that the observed phenomenon happens for various visible wavelengths and at very low powers, has an abrupt turn-on transition at the threshold, and the fact that nanotube forests are easy and inexpensive to make and can potentially be operated in modest vacuum conditions with high stability and lifetime, the effect has important implications for optical absorbers and detectors, optical switching and modulation devices, thermopower wave guides [83], vacuum-based solar energy harvesters [84], solar electron sources for a multitude of applications such as display technologies, laser-assisted nanostructure growth [85], and thermoelectric devices [86]. It will be interesting to see whether similar effects also occur in other nanostructured systems such as

5.4. Summary

various nanowires or graphene.

Chapter 6

Temperature-Dependant Quantum Efficiency and Transition from Photoemission to Thermionic Emission in Carbon Nanotube Arrays Under Low-Power Ultraviolet Illumination

The effect of heat on photoemission or light on thermionic emission has been of interest and studied since the times of Fowler and DuBridge [18, 87], but typically such studies are done using a substrate heater in addition to the light source. Recently, there is renewed interest in these effects for new device applications such as solar cells. For example, Schwede *et al.* proposed photon-enhanced thermionic emission for novel vacuum photovoltaics [5].

Here we present a case where both photoemission and thermionic emission happen using a low-power, continuous-wave, ultraviolet laser. We see that there is photoemission and the emission current is linearly dependent on laser power (also demonstrated in chapter 3) and the quantum efficiency is constant. As the laser

The material presented in this chapter is in preparation for submission as a journal article

intensity increases, the illuminated spot on the nanotube forest gradually becomes warmer, the quantum efficiency gradually changes and the current-vs.-temperature curve follows the Fowler-duBridge model for thermally-assisted photoemission [18, 87]. Eventually, there is a transition from photoemission to thermionic emission and, beyond this transition point, a small increase in laser power increases the temperature drastically and, as a result, increases the emission current, which is now dominated by thermionic emission.

The observed emission characteristics as a function of power are different than the visible-light heating of CNT arrays (demonstrated in chapters 4 and 5), where there was no photoemission regime.

6.1 Methodology

Figure 6.1(a) illustrates the experimental setup, which is similar to the setup in chapter 3 except that a lens is used to focus the ultraviolet beam and Figure 6.1(b) illustrates the beam spot on the sidewall of the CNT forest. The CNT samples for this experiment were grown using the second generation CVD system, which is discussed in chapter 2.

6.2 Results and Discussion

The electron emission current as a function of laser power is illustrated in Figure 6.2 for two cases. Figure 6.2(a) was obtained with a wider laser spot than Figure 6.2(b), therefore corresponding to lower intensities for the same level of power. We observed a repeatable behaviour on different CNT samples and on different parts of the sidewall of each CNT sample.

This behaviour is different than what was reported in chapter 3 where the entire nanotube forest was flooded with an unfocused ultraviolet beam. There, the laser intensity was significantly lower, and a simple photoemission behaviour was observed with emission current being a linear function of laser power.

We also measured the emission temperature of the incandescent spot by recording the spectrum and fitting it to Planck's black-body radiation law. The measurements were limited to temperatures higher than $\sim 1,500$ K due to the wavelength limitation of the spectrometer. Using the power equilibrium equation (equation 5.1) we also calculated the temperature in this range and below 1,500 K and compared it to our measured results (Figure 6.3). This illustrates the efficient heating of

6.2. Results and Discussion

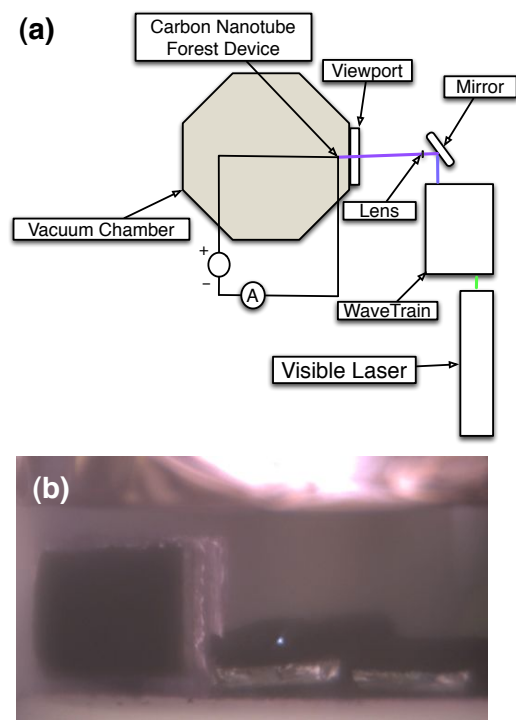


Figure 6.1: (a) Experimental setup where the laser is focused onto the CNT sidewall. (b) Laser spot on the CNT forest sidewall.

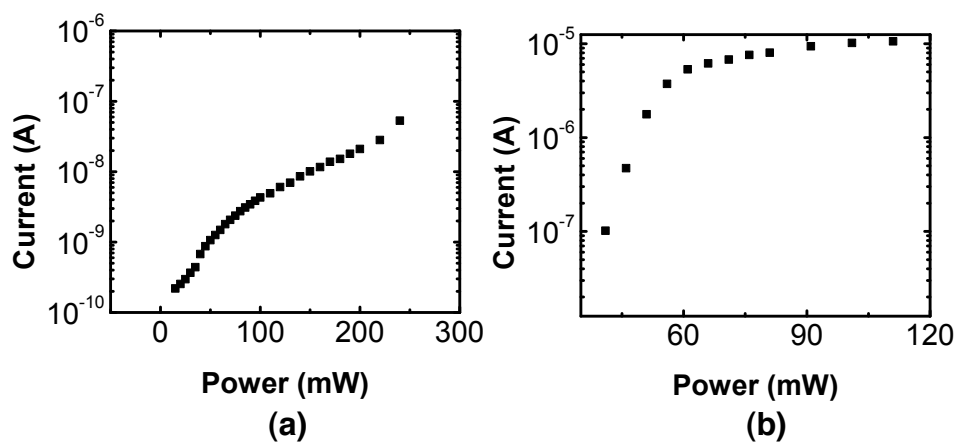


Figure 6.2: (a) Emission current as a function of power for low intensity laser. (b) Emission current as a function of power for high intensity laser.

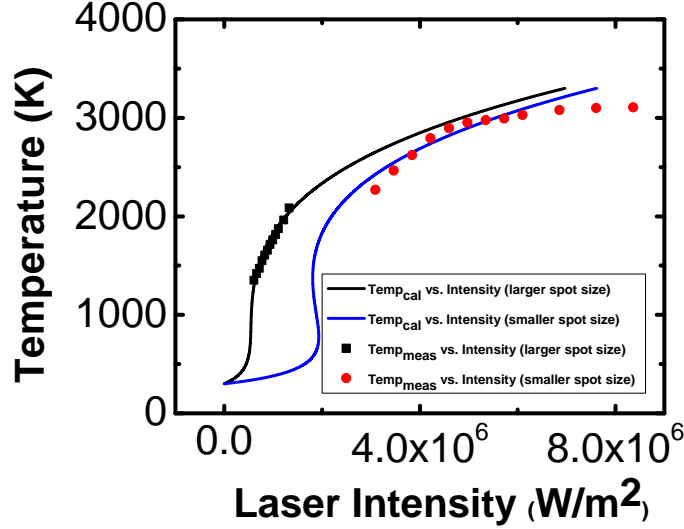


Figure 6.3: Temperature as a function of laser intensity. The parameters for calculating the temperature for the solid lines were: $r = 240 \mu\text{m}$ for the larger spot size (black line) and $r = 65 \mu\text{m}$ for the smaller spot size (red line), $\epsilon = 1$, $\Phi = 4.652 \text{ eV}$, $L = 14 \mu\text{m}$, $T_{\text{room}} = 300 \text{ K}$, and the depth of the hot area for calculating A_{heat} was $\sim 50 \text{ nm}$.

nanotube arrays with low ultraviolet laser powers, which can again be contributed to the “Heat Trap” effect that we have discovered in chapter 5.

For temperatures where the spectrum could be recorded for both cases of the low and high intensities, the estimated temperatures from the spectra are in good agreement with the calculated temperatures using the power equilibrium equation (shown in Figure 6.3).

Figure 6.4 illustrates the emission current as a function of calculated and measured temperatures for both laser spot sizes (Figure 6.2(a) and Figure 6.2(b)). The temperature was calculated using equation 5.1. Measurable emission currents at low laser intensities were not present in our visible-light experiments (chapters 4 and 5), indicating that the photon energy of the laser also has an effect in this region.

Figure 6.4 also shows the the Fowler-DuBridge model (discussed in section 1.2.3) fitted to the measured results. The model shows a good fit with the measured emission current, which illustrates that not only the ultraviolet laser is causing photoemission, it is also heating up the carbon nanotubes simultaneously. This

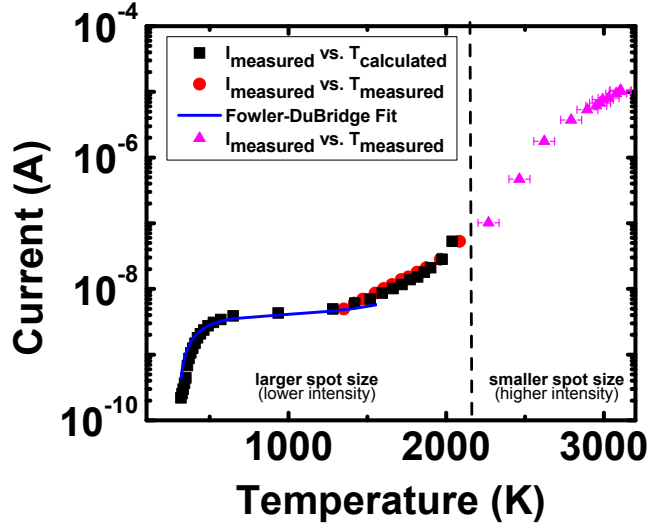


Figure 6.4: Emission current as a function of temperature. (Note that the two separate parts of the curve were obtained in two different experiments and should be considered separately.) The parameters for calculating the temperatures (square markers) using equation 5.1 were: $r = 240 \mu\text{m}$, $\epsilon = 1$, $\Phi = 4.652 \text{ eV}$, $L = 14 \mu\text{m}$, $T_{\text{room}} = 300 \text{ K}$, and the depth of the hot area for calculating A_{heat} was $\sim 50 \text{ nm}$. The parameters for calculating the current using the Fowler-DuBridge model (equation 1.6) were: $\alpha = 11e-8$, $E_{\text{photon}} = 4.66 \text{ eV}$, and $\Phi = 4.652 \text{ eV}$. The input power was corrected for the transparency of the sapphire viewport (70% at 266 nm).

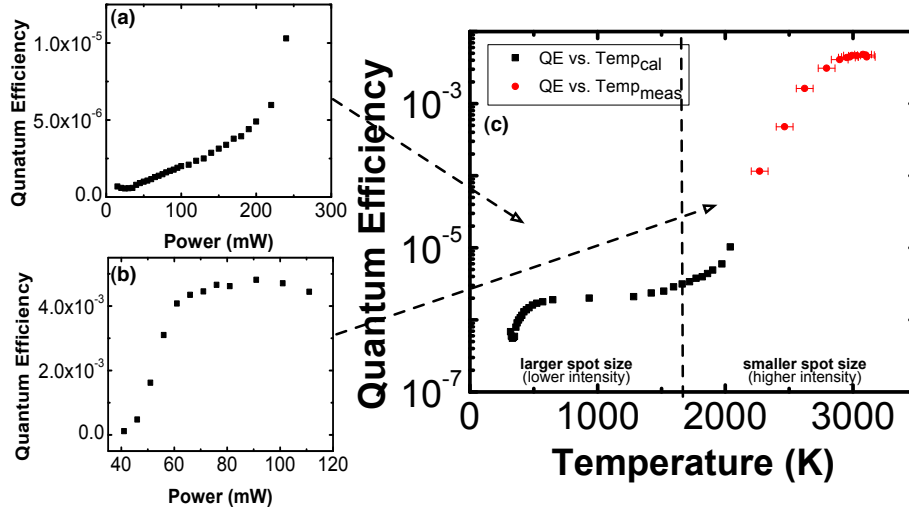


Figure 6.5: (a) Quantum efficiency as a function of power for low laser intensity. (b) Quantum efficiency as a function of power for high laser intensity. (c) Quantum efficiency as a function of temperature (Note that the two separate parts of the curve were obtained in two different experiments and should be considered separate).

observed heating effect with such low amount of laser intensity is again unique since in bulk conductors (such as tungsten) laser intensities as high as 1 GWcm^{-2} are required to achieve a temperature rise of $\sim 600 \text{ K}$ [88]. All of the experiments that illustrate the effect of temperature on photoemission either use a substrate heater or are under irradiation with a pulsed laser, which have very high intensities ($> 1 \text{ GWcm}^{-2}$).

Figure 6.5 illustrated the quantum efficiency (QE) as a function of laser power (Figure 6.5(a) and (b)) and temperature (Figure 6.5(c)). QE increases as a function of temperature, shows a non-linear behaviour and approaches to $\sim 1\%$ at 3,000 K.

The rapid increase of the electron emission current as a function of temperature at temperatures above 2,000 K (see Figure 6.4) can be explained as thermionic emission as it has the same slope (Figure 6.6) as Richardson-Dushman's equation. This behaviour is similar to our previous observation (also illustrated on Figure 6.6), which was for a green laser (discussed in chapter 5). The saturation of emission current at high temperatures can be due to a combination of CNT destruction and the space-charge effect.

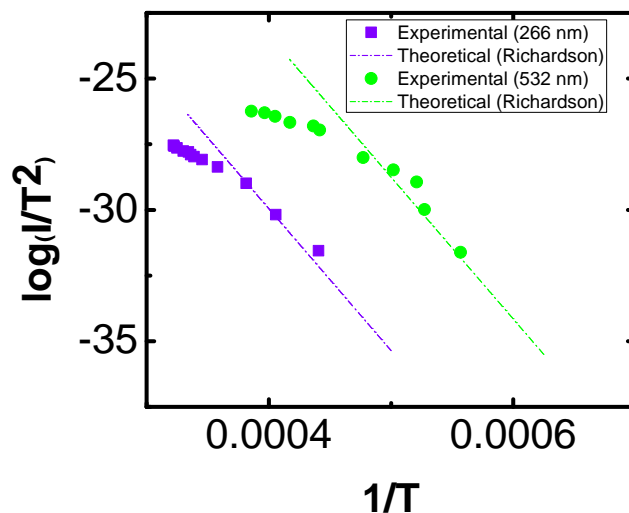


Figure 6.6: Emission current as a function of temperature on the Richardson axis for UV and green lasers.

6.3 Summary

Arrays of millimetre-long CNTs were irradiated by a focused beam of ultraviolet laser. The observed effect at low laser intensities was consistent with our earlier observation of flood irradiation with an ultraviolet laser in chapter 3 but started to deviate from it as the laser intensity was increased. It appears that the “Heat Trap” effect, which leads to the rapid increase of temperature in the CNT array, is also strongly present in the ultraviolet spectrum.

Chapter 7

Broadband Light-Induced Thermionic Electron Emission from Arrays of Carbon Nanotubes using Laser Pointers

As mentioned in the introduction, photocathodes either require high-energy photons (ultra-violet) or have to be made from semimetals/semiconductors combined with alkali metals to have low workfunction in order to operate with visible light. The former suffer from the challenges associated with ultra-violet sources and the latter are highly unstable and can only operate in ultra-high vacuum conditions (better than 10^{-10} Torr). High-power pulsed lasers (with a few GWcm^{-2} of light intensity) are also used for thermionic emission from metals, but again require a sophisticated and expensive light source. In this chapter, we show that a photocathode made from an array of carbon nanotubes (a nanotube forest) can address all of these challenges.

In chapters 4 and 5, we discussed thermionic emission from carbon nanotube forests induced by collimated and focused beams of continuous-wave, visible lasers. In those studies, we had used research grade lasers (an argon ion laser and a solid-state laser) with a small range of wavelengths (488 nm - 532 nm). In this chapter, we demonstrate electron emission from nanotube forests using continuous-wave, battery-operated, hand-held lasers with four different wavelengths in a broad visible/infrared range (405 nm, 532 nm, 650 nm, and 1064 nm) and demonstrate the

A version of this chapter has been presented at the 55th international conference on electron, ion, and photon beam technology and nanofabrication. [89]

7.1. Methodology

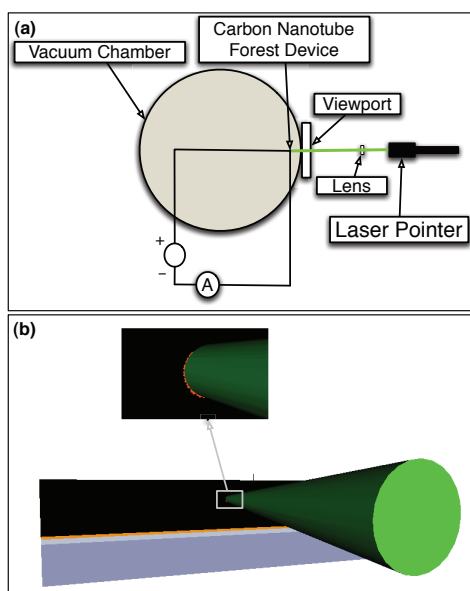


Figure 7.1: Schematic of the experimental apparatus using a laser pointer where the beam is focused with a lens, placed outside of the vacuum chamber, on the sidewall of the nanotube forest through a sapphire viewport.

operation of the device in poor vacuum conditions.

7.1 Methodology

The nanotube forests were grown using the second generation CVD system and mounted on a sample holder and placed in a high vacuum chamber ($\sim 10^{-8}$ Torr). The forests were used as the cathode and a copper anode was placed a few millimetres above the cathode. The handheld lasers used were from Laserglow technologies with the following model numbers: Electra Pro-40 (405 nm), Aries-35 (532 nm), Orion-200 (658 nm), and Scorpius-500 (1064 nm). Figure 7.1 illustrates the experimental configuration.

Upon irradiation by a laser beam with enough intensity, the illuminated spot on the nanotube forest surface exhibited a bright incandescent glow, accompanied by electron emission (as discussed previously).

7.2 Results and Discussion

Figure 7.2 illustrates the electron emission current as a function of laser power for the four different wavelengths. In all cases, the emission-current has a non-linear relationship with laser-power (see insets of Figure 7.2). We observe that significant electron emission takes place regardless of the laser wavelength, suggesting that a broad range of lasers can be used for a nanotube-based thermionic electron-source. It should also be noted that since the emission process is primarily not wavelength dependent, one expects that a regular wide-spectrum light source could also be used. This has important implications for bringing photocathodes to mainstream applications such as solar energy conversion and displays.

The temperature of the emission spot can again be estimated using the power equilibrium equation (equation 5.1). Figure 7.3 shows the emission current as a function of the temperature estimated in this manner. A theoretical estimate based on the Richardson equation for thermionic emission is also shown, providing a reasonable fit to the experimental data.

The effect of combined wavelengths can be demonstrated by focusing the different beams onto a single spot (Figure 7.4). As illustrated in table 7.1, the emission current due to the combination of the laser beams is much higher than the sum of currents resulting from each laser independently. For example, the emission current due to the combination of green and red is about 2 orders of magnitude higher than the currents due to red and green added together. Such non-linearity is, of course, expected in thermionic emission, where the addition of a small amount of laser power and corresponding rise in temperature could lead to a significant increase in current. To further illustrate this point, Figure 7.5 shows the emission current as a function of calculated temperature using the power equilibrium equation (equation 5.1) and Richardson's equation (equation 1.4). In order to estimate the temperature for the combination of Green + Red and Green + Red + Violet, only the power of the different wavelength lasers were used. For example, to estimate the temperature of the Green + Red combination the laser power of 45 mW +150 mW was used. As it can be seen in Figure 7.5 the trend of increase in current for the different combinations of lasers follows the trend of Richardson's equation. This indicates that adding different laser wavelengths simply acts as adding the power of those lasers together. This behavior should be expected since CNTs do have a relatively constant coefficient of optical absorption across the visible range.

As mentioned earlier, one of the challenges of photocathodes is high-vacuum requirements. For example, photocathodes with high quantum efficiencies can only

7.2. Results and Discussion

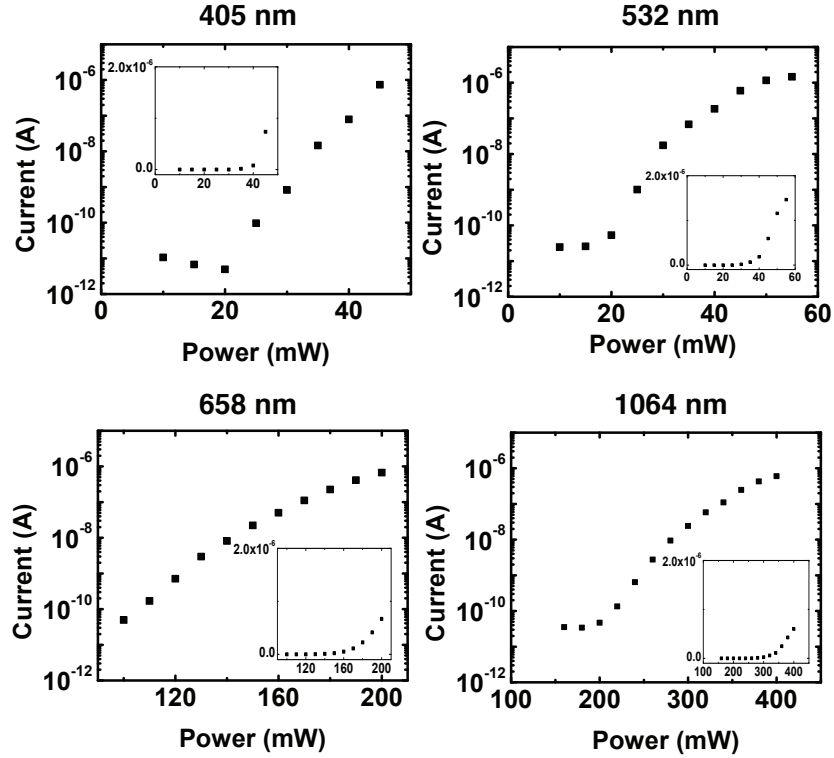


Figure 7.2: Electron emission current as function of laser power for laser wavelengths of 405 nm, 532 nm, 658 nm, and 1064 nm. In all cases the laser was focused to a spot in the range of 200 - 600 μm in diameter. Since this emission process depends on the light intensity, the beam shape of the laser can greatly affect the emission current for a given laser power. In the 658 nm and 1064 nm cases, the laser beams were overall wider, less circular and more difficult to focus, and therefore more laser power was needed for electron emission. Insets: nonlogarithmic plot for each wavelength.

Table 7.1: Emission currents as a result of individual lasers and their combination.

Wavelength	Emission Current	Power	Spot Diameter (estimate)
Violet	14 nA	40 mW	250 μm
Green	33 nA	45 mW	200 μm
Red	1.5 nA	150 mW	400 μm
G + R	2.2 μA	×	×
G + R + V	9 μA	×	×

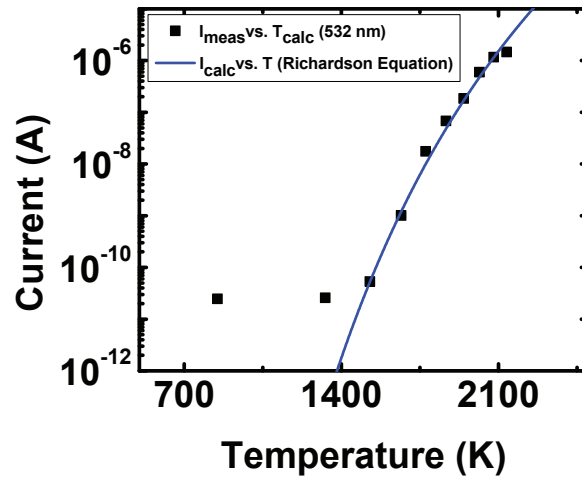


Figure 7.3: Electron emission current as a function of estimated temperature using a power equilibrium equation. The measured data follow the thermionic emission behaviour predicted by the Richardson equation. The minimum measurement limit with our experimental setup is tens of picoamperes. The parameters for calculating the temperatures (square dots) using equation 5.1 are: $r = 115 \mu\text{m}$, $\epsilon = 1$, $\Phi = 4.652 \text{ eV}$, $L = 80 \mu\text{m}$, $T_{room} = 300 \text{ K}$, and the depth for calculating A_{heat} was $\sim 50 \text{ nm}$.

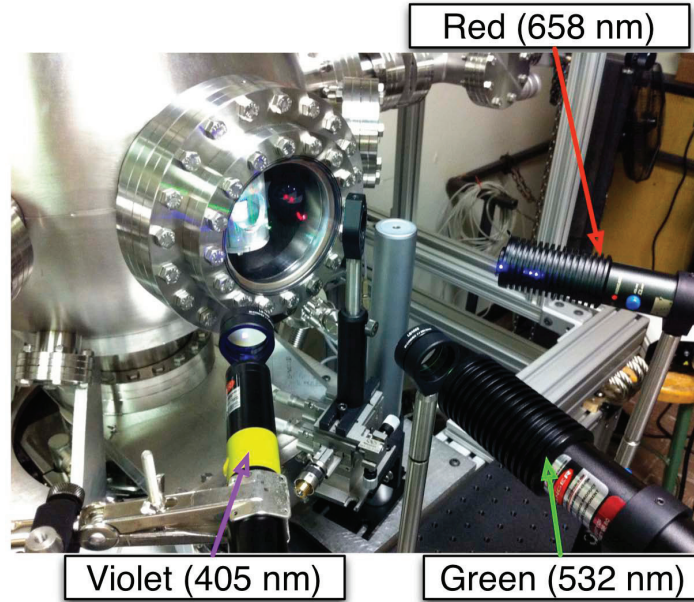


Figure 7.4: Multiple laser beams with different wavelengths being focused onto a single spot.

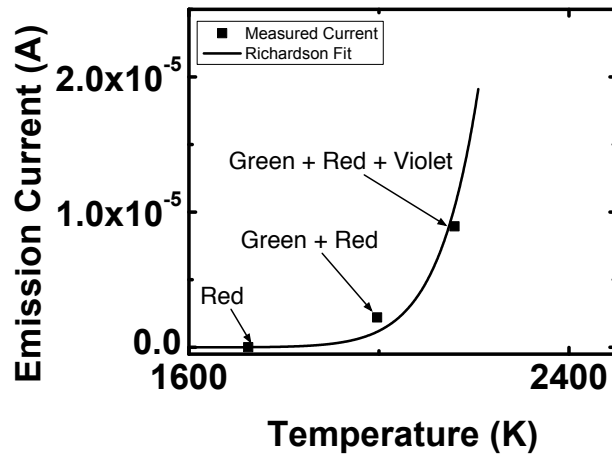


Figure 7.5: Emission current as a function of temperature for different combinations of laser wavelengths. The parameters for calculating the temperatures (square dots) using equation 5.1 are: $r = 215 \mu\text{m}$, $\epsilon = 1$, $\Phi = 4.652 \text{ eV}$, $L = 14 \mu\text{m}$, $T_{room} = 300 \text{ K}$, and the depth for calculating A_{heat} was $\sim 50 \text{ nm}$.

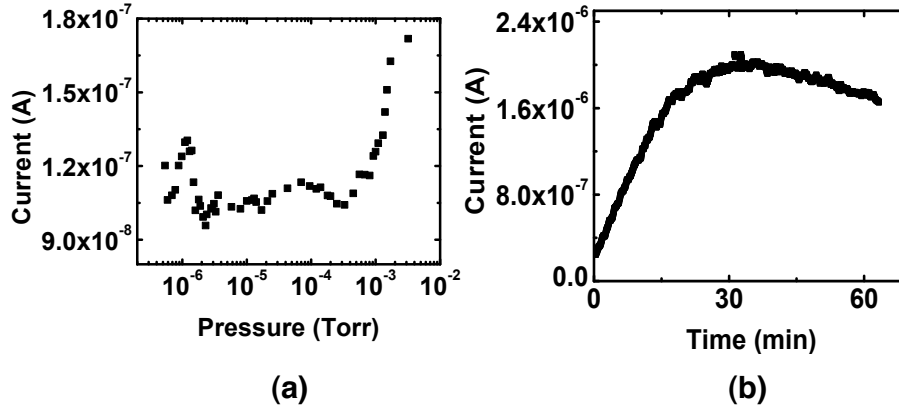


Figure 7.6: (a) Emission current as a function of pressure. (b) Emission current as a function of time at a pressure of $\sim 5 \times 10^{-3}$ Torr. The laser had a wavelength of 532 nm, spot diameter of $\sim 200 \mu\text{m}$ and power of 50 mW.

operate reliably in pressures lower than 10^{-10} Torr. Figure 7.6(a) shows the emission current from the nanotube forest as a function of the vacuum level (controlled using nitrogen) for the laser wavelength of 532 nm. Other than the initial jump in current and the increasing trend at higher pressures, the current only fluctuates about 15% in a wide range of pressures. Figure 7.6(b) illustrates the emission current when the pressure is held constant at about 5×10^{-3} Torr for about one hour. The emission current slowly rises, saturates at about $2 \mu\text{A}$ and then decreases very slowly. Although a detailed study is needed to characterize and understand the effect of vacuum level on these sources, these preliminary data clearly show the potential of these devices to operate in poor vacuum.

7.3 Summary

We demonstrated that carbon nanotube forests can act as thermionic electron sources, excited by inexpensive, handheld lasers with a variety of wavelengths ranging from visible to infrared. These arrays can operate even in poor vacuum conditions and be relatively stable. These properties of nanotube forests can open the door to various vacuum electronic applications.

Chapter 8

Increasing the Current Density of Light-Induced Thermionic Electron Emission from Carbon Nanotube Arrays

In this chapter we demonstrate how to increase the current density of a light-induced thermionic emitter, based on CNT arrays, and its performance in modest vacuum levels.

8.1 Methodology

Millimeter-long arrays of vertically aligned multiwalled CNTs were illuminated on their sidewall by a focused green (532-nm) laser beam (power of up to several 100mW). The hot spot created due to the “Heat Trap” effect was imaged using a Navitar Zoom 6000 lens system with a CCD camera. Figure 8.1 shows a schematic of the experiment and an optical micrograph of the incandescent glow of the electron emission spot on the forest sidewall.

The emission current was recorded as a function of laser power and the black-body radiation spectrum was measured in each case to find the emission spot temperature. Since a CNT forest consists of $\sim 90\%$ empty space, the sidewall of CNTs occupy only a small percentage of the laser spot and presumably, a significant portion of the laser energy is wasted. We increased the forest density by placing a

A version of this chapter has been presented at the 24th international vacuum nano-electronics conference. [90]

8.2. Results and Discussion

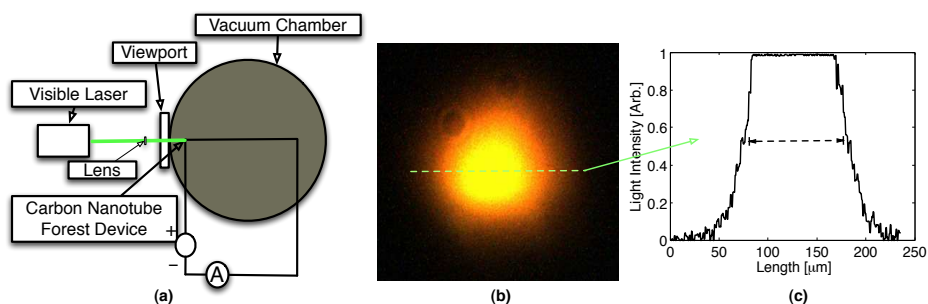


Figure 8.1: (a) Experimental apparatus. (b) Image of the emission spot with the laser light filtered out. (c) Cross-section of the emission spot showing its diameter.

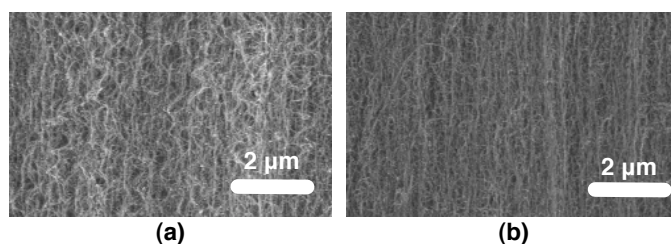


Figure 8.2: Scanning electron micrographs of as-grown (a) and densified (b) CNT arrays.

small amount of isopropyl alcohol on it. The liquid flowing through the forest pulls the nanotubes closer together and makes the forest denser (Figure 8.2).

8.2 Results and Discussion

Figure 8.3(a) shows the emission current density versus emission spot temperature for as-grown and densified arrays, the latter showing an increase of up to 4 times. Interestingly, beyond $\sim 3,100\text{K}$, the current density of the as-grown sample declines, whereas that of the densified forest keeps increasing, suggesting that the latter is more robust and can withstand higher temperatures, presumably due to the tighter packing of the CNTs. In the stability test (Figure 8.3(b)), the current density initially drops in both cases, but eventually stabilizes after $\sim 20\text{-}40\text{min}$, though at a much higher value for the densified sample.

We also measured the emission current as a function of vacuum level to see the stability of the densified CNTs. Figure 8.4(a) shows that the densified CNTs remain

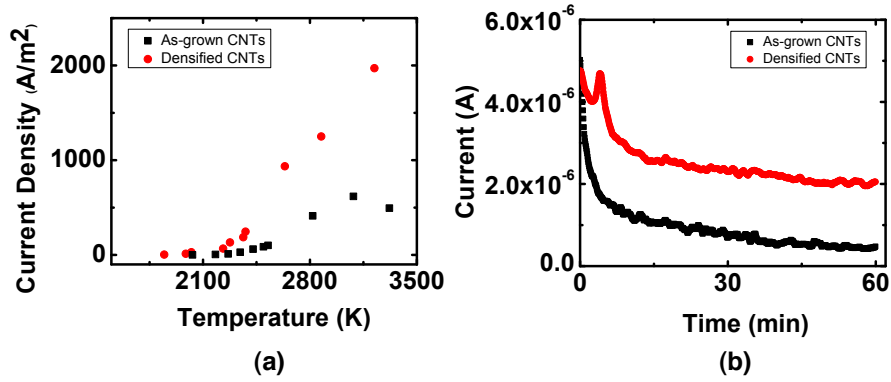


Figure 8.3: Emission current density vs. temperature for the as-grown and densified CNT arrays. (b) Emission current as a function of time for both cases.

stable (with less than 10% of fluctuation) as the pressure is increased. Similar to the case of as-grown sample (Figure 7.6), the electron emission current increases as pressure increases beyond 10^{-3} Torr. The emission current keeps on increasing and saturates for about 15 minutes as the pressure is maintained at about 5×10^{-3} Torr and then starts to slowly decrease (Figure 8.4(b)).

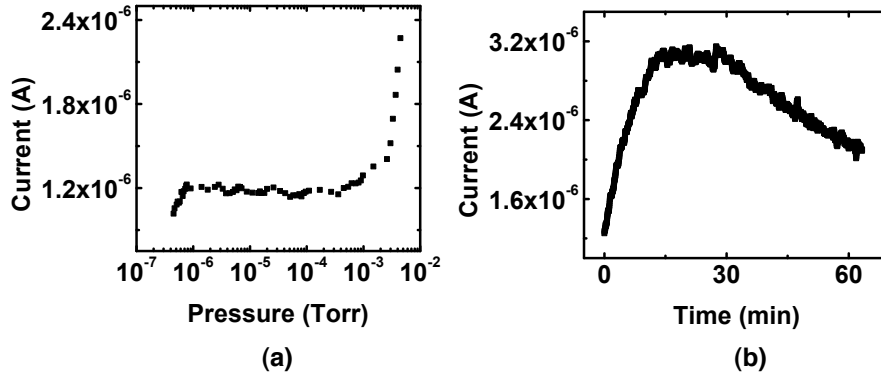


Figure 8.4: (a) Emission current as a function of vacuum level for incident laser wavelength of 532 nm. (b) Emission current stability over time at a pressure of $\sim 5 \times 10^{-3}$ Torr.

This simple densification technique can be further exploited to make the nanotube forest even denser. By micro patterning small islands of such nanotube

forests, one can shrink them even more and create thin pillars for efficient microstructured photo-electron source arrays.

8.3 Summary

The current density of a photocathode is an important performance parameter when it comes to any potential application. In this work, we demonstrated that by a simple densification technique we can increase the current density of the arrays of CNTs by about 4 times. This current density is still below the current state-of-the-art photocathodes but by growing the nanotube arrays in a small area, this densification technique can further pack the nanotubes and potentially increase the current density even further. These thin pillars can also be used as arrays of electron sources for flat panel displays.

Chapter 9

Conclusion

Before this work, there were only a limited number of studies that investigated light-induced electron emission from CNTs for electron source applications. This thesis describes light-induced electron emission from arrays of CNTs with a broad range of wavelengths and light intensities. The observations in this thesis demonstrate unique characteristics, such as the “Heat Trap” mechanism, which not only have implications for existing electron-source technologies, but they can also open the door to novel applications such as new solar cells (discussed later in this chapter). A summary of the contributions of this thesis, along with some ideas for future work, is presented in this chapter.

9.1 Contributions

The contributions of this thesis and their immediate applications are listed below:

1. Chapter 2 describes a growth system for nanotube forest and the experimental setup required for characterizing electron emission from nanotube electron sources. The developed growth technique is quite repeatable and can be used for many different applications. For example, nanotubes that were grown with this technique are currently being used by other UBC graduate students in experiments such as characterizing secondary electron emission from nanotubes [91], electro discharge machining of nanotube forests [92], and developing novel pressure sensors [93]. This growth method gives researchers the ability to use nanotubes at a macroscopic scale.
2. Chapter 3 details the experimental evidence for a nanotube based photocathode with a high quantum efficiency of $> 10^{-5}$. The potential application of these photocathodes would be to replace current metal photocathodes. This is because CNTs, because of their chemically stable structure, are more robust than bulk metals, which are unstable because of dangling bonds on their surface. Moreover, the unique internal structure of the nanotube forest can

be exploited for novel applications, which are not possible with conventional metals. For example, nanotube forests are sensitive to the polarization of light, so a polarization-dependent photocathode switch operating at gigahertz speeds can potentially be developed.

3. Chapter 4 reports of nanotube-based light-induced electron thermionic source that can operate with relatively low light intensity. It also provides some evidence for a possible photo-field emission process. These two different regions of operation, which are distinguished by the applied electric field and light intensity, can be used for increased control in electron emission. This is because nanotubes have an inherent high-aspect-ratio structure, allowing them to operate using much smaller applied external fields, and lower laser intensities than conventional metals. This means that cheaper and smaller electronics and lasers are required and allows the development of more compact vacuum electronic devices.
4. Chapter 5 illustrates that the power of the collimated beam (in Chapter 4) that is required for light-induced thermionic emission can be further reduced by using a lens to focus the light. This is because the heat generated from the incident light is trapped and cannot dissipate. This “Heat Trap” effect can be explained by a rapid drop in thermal conductivity of nanotubes at high temperatures and the anisotropic nature of the structure of the forest. The behaviour is different in bulk conductors, which can dissipate the heat generated by the incident light even at high temperatures. This efficient heating of nanotubes has important implications in light-induced thermionic electron sources. For example, the cost of building a light-induced thermionic source can be significantly reduced because inexpensive, low-power lasers can be used for nanotubes as apposed to high-power or pulsed laser sources, which are required for metal cathodes.
5. Chapter 6 describes the effect of high energy photons (UV laser) and self heating due to the laser. It turns out that laser-induced heating is also present in the photoemission regime of nanotubes, which is not measurable in experiments with smaller photon energies (chapter 4 and 5) or experiments with the same photon energy but much lower light intensities (chapter 3). Also, heating in the photoemission regime with such low-laser intensities has not been observed in other materials.
6. Chapters 7 and 8 show the broadband nature of light-induced thermionic emission and how to increase the current density of the nanotube-based elec-

tron sources, respectively. These two characteristics are very important for any existing or new electron source application. For example, existing light-induced thermionic sources have a specific built-in laser, so without having to change the laser, nanotube based cathodes can be fitted in such systems. Also, the telecommunications industry has driven down the cost of production of lasers of specific wavelengths (for example 850 nm or 1550 nm) and, because of the broadband and low-light-power nature of these nanotube electron sources, inexpensive cathodes could be developed and integrated on chip for applications such as optoelectronic switches .

9.2 Future Work

The “Heat Trap” behaviour in nanotube forests can address some of the challenges in photocathodes and it can also be exploited for novel applications ranging from optical detectors to solar-energy harvesters and solar displays.

The reported observations should also motivate further fundamental investigation into this behaviour. Of course, this can be a difficult task since, even after 20 years of research on nanotubes, because of their nanoscale dimensions and inconsistent growth of individual nanotubes, there is still no consensus on some of their physical properties. For example, properties such as the workfunction and thermal conductivity of nanotubes are still being investigated even though a great amount of research has been done already. The proposed power equilibrium model has tried to explain the observed behaviour with bulk properties such as using the bulk Richardson constant and assuming that the Stephen-Boltzmann law hold for nanotubes. Although this model shows good agreement with the measured results, a more fundamental understating of this effect is required. The observed behaviour is very interesting and unique to nanotubes; therefore, our observations should also motivate the investigation of other nanostructures for this behaviour. More importantly, our observations may prompt others to probe the potential of this phenomenon for real world applications.

For further fundamental study of this effect such experiments as measuring the energy spectrum of the emitted electrons at different laser wavelengths will provide great insight into the emission mechanism. Also, other experiments such as Raman spectroscopy with high laser intensities might give insight into the electron-phonon coupling that may be responsible for such localized heating.

There are not many materials, including nanomaterials, that can withstand thermionic emission temperatures. Researchers have developed growth techniques

for tungsten nanowires that are a few micrometers long but are in a sparse form[94]. These short sparse nanowires, of course, have a different structure than our dense, millimeter-long CNTs and there will be some optical challenges in focusing a laser beam to such a small space; nevertheless, testing such nanowires will be interesting in further understanding of this phenomenon.

9.2.1 Solar Electron Source

One of the most abundant sources of light is the sun, which has an average insolation (solar radiation energy received on a given surface) of about 1 kWm^{-2} and perhaps the most immediate application of our findings is a sunlight-activated electron source.

The basis of a solar electron source is very simple and easy to discuss given our results. The solar radiation spectrum ranges from ultraviolet ($\sim 250 \text{ nm}$) to infrared ($\sim 2,000 \text{ nm}$) with the highest peak of irradiance at around 500 nm . This is in the same range of wavelengths as where we have demonstrated thermionic emission from the CNT forests (266 nm to 1064 nm). If we place a typical lens (with 1 inch in diameter) in the sunlight, it will receive an incident radiation of 500 mW of sunlight. This amount of power, given the majority of it being in the visible wavelength range, when focused to a $200 \mu\text{m}$ spot is more than enough to cause electron emission from the CNT forests.

Of course this emission process is highly intensity dependent and the chromatic aberration of the lens and the wide spectrum of sunlight as compared to a laser light, will be the biggest concern in being able to focus enough light to cause electron emission. This problem has a few existing solutions such as reducing the chromatic aberration by coating the lens with thin film or using an achromatic doublet. The collected radiation of the sunlight can also be increased by using a lens with a bigger surface area or using a concave mirror to collect and focus more solar radiation. Since the power required (a few 10s of mW) is very low, either of the above solutions will be simple and inexpensive to implement.

The sunlight can also be put into lensed fibers where each fiber is mounted close to a pillar of densified CNTs in the shape of a sharp needle and an array of these needles could be used (as discussed in the previous chapters) for solar flat panel displays.

9.2.2 Solar Cell

As mentioned above, the amount of sun that is incident on earth is more than enough to cause electron emission from these nanotube forests. Also, recently, photo-enhanced thermionic emission-based solar cells using solar concentrator systems have been proposed [5]. However, existing candidate photocathodes are very sensitive and cannot operate at high temperatures like nanotube forests. A nanotube based solar cell can be designed based on the observed effect. The concentrated sun (either by mirrors or lens) can heat up the nanotubes to high enough temperatures where the electrons would overcome the workfunction of the nanotubes. These free electrons now have to flow to the anode so that an electron flow (or a current) can be generated. In photovoltaics the holes and the electrons separate and start to flow because of the built in voltage of the p-n junction. A similar idea can be implemented here; if the anode has a smaller workfunction than the nanotubes, once a load is connected (such as a piece of wire) between the anode and the cathode, the fermi energies would line up, which would bend the vacuum level (as shown in Figure 9.1). This would accelerate the emitted electrons towards the anode and a current would be measured. This proposed thermionic solar harvester can be the foundation of a new generation of solar cells.

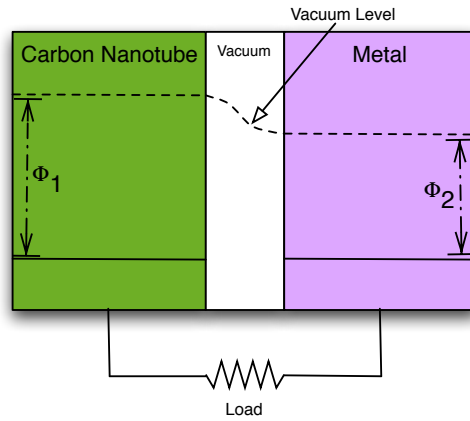


Figure 9.1: Band diagram of a solar-cell configuration of nanotubes.

Bibliography

- [1] Zu-Po Yang, Lijie Ci, James A. Bur, Shawn-Yu Lin, and Pulickel M. Ajayan. Experimental observation of an extremely dark material made by a low-density nanotube array. *Nano Letters*, 8(2):446–451, 2008.
- [2] Kohei Mizuno, Juntaro Ishii, Hideo Kishida, Yuhei Hayamizu, Satoshi Yasuda, Don N. Futaba, Motoo Yumura, and Kenji Hata. A black body absorber from vertically aligned single-walled carbon nanotubes. *Proceedings of the National Academy of Sciences*, 106(15):6044–6047, 2009.
- [3] R. Brogle, P. Muggli, P. Davis, G. Hairapetian, and C. Joshi. Studies of linear and nonlinear photoelectric emission for advanced accelerator applications. volume 2, pages 1039 –1042, may. 1995.
- [4] S. H. Kong, J. Kinross-Wright, D. C. Nguyen, and R. L. Sheffield. Photocathodes for free electron lasers. *Nuclear Instruments and Methods in Physics Research Section A: Accelerators, Spectrometers, Detectors and Associated Equipment*, 358(1-3):272 – 275, 1995. Proceedings of the Sixteenth International Free Electron Laser Conference.
- [5] Jared W. Schwede, Igor Bargatin, Daniel C. Riley, Brian E. Hardin, Samuel J. Rosenthal, Yun Sun, Felix Schmitt, Piero Pianetta, Roger T. Howe, Zhi-Xun Shen, and Nicholas A. Melosh. Photon-enhanced thermionic emission for solar concentrator systems. *Nat Mater*, 9(9):762–767, 09 2010.
- [6] J. P. Girardeau-Montaut, C. Girardeau-Montaut, S. D. Moustazis, and C. Fotakis. High current density produced by femtosecond nonlinear

Bibliography

- single-photon photoelectric emission from gold. *Applied Physics Letters*, 62(4):426–428, jan. 1993.
- [7] R. Ganter, R. Bakker, C. Gough, S. C. Leemann, M. Paraliiev, M. Pedrozzi, F. Le Pimpec, V. Schlott, L. Rivkin, and A. Wrulich. Laser-photofield emission from needle cathodes for low-emittance electron beams. *Phys. Rev. Lett.*, 100(6):064801, Feb 2008.
- [8] Brett Barwick, Hyun Soon Park, Oh-Hoon Kwon, J. Spencer Baskin, and Ahmed H. Zewail. 4D Imaging of Transient Structures and Morphologies in Ultrafast Electron Microscopy. *Science*, 322(5905):1227–1231, 2008.
- [9] Bradley J. Siwick, Jason R. Dwyer, Robert E. Jordan, and R. J. Dwayne Miller. An Atomic-Level View of Melting Using Femtosecond Electron Diffraction. *Science*, 302(5649):1382–1385, 2003.
- [10] R. H. Fowler; L. Nordheim. Electron emission in intense electric fields. *Proceedings of the Royal Society of London. Series A, Containing Papers of a Mathematical and Physical Character*, 119(781):173–181, 1928.
- [11] E. L. Murphy and R. H. Good. Thermionic emission, field emission, and the transition region. *Phys. Rev.*, 102(6):1464–1473, 1956.
- [12] L.W. Swanson and A.E. Bell. Recent advances in field electron microscopy of metals. volume 32 of *Advances in Electronics and Electron Physics*, pages 193 – 309. Academic Press, 1973.
- [13] C.A. Spindt, C.E. Holland, A. Rosengreen, and I. Brodie. Field-emitter arrays for vacuum microelectronics. *Electron Devices, IEEE Transactions on*, 38(10):2355 –2363, 1991.
- [14] Walt A. de Heer, A. Châtelain, and D. Ugarte. A carbon nanotube field-emission electron source. *Science*, 270(5239):1179–1180, 1995.
- [15] O. W. Richardson. Temperature variation of electronic emission. *Camb. Phil. Proc.*, 11:286, 1901.

- [16] F. Wooten and R. N. Stuart. Fowler's hypothesis and the determination of photoemission thresholds. *Phys. Rev.*, 186:592–593, 1969.
- [17] V. Nassisi, A. Beloglazov, E. Giannico, M. R. Perrone, and A. Rainò. Emission and emittance measurements of electron beams generated from cu and diamond photocathodes. *Journal of Applied Physics*, 84(4):2268–2271, 1998.
- [18] R. H. Fowler. The analysis of photoelectric sensitivity curves for clean metals at various temperatures. *Physical Review*, 38:45–56, 1931.
- [19] Kevin L. Jensen, Donald W. Feldman, Matt Virgo, and Patrick G. O'Shea. Measurement and analysis of thermal photoemission from a dispenser cathode. *Phys. Rev. ST Accel. Beams*, 6:083501, Aug 2003.
- [20] Mark J. Hagmann. Resonance due to the interaction of tunneling particles with modulation quanta. *Applied Physics Letters*, 66:789–791, 1995.
- [21] Peter Hommelhoff, Yvan Sortais, Anoush Aghajani-Talesh, and Mark A. Kasevich. Field emission tip as a nanometer source of free electron femtosecond pulses. *Phys. Rev. Lett.*, 96(7):077401, Feb 2006.
- [22] Hirofumi Yanagisawa, Matthias Hengsberger, Dominik Leuenberger, Martin Klöckner, Christian Hafner, Thomas Greber, and Jürg Osterwalder. Energy distribution curves of ultrafast laser-induced field emission and their implications for electron dynamics. *Phys. Rev. Lett.*, 107:087601, 2011.
- [23] Markus Schenk, Michael Krüger, and Peter Hommelhoff. Strong-field above-threshold photoemission from sharp metal tips. *Phys. Rev. Lett.*, 105:257601, 2010.
- [24] Csaba Beleznai, Dominique Vouagner, and Jean-Pierre Girardeau-Montaut. Evidence of surface structural transformations during pulsed uv laser-induced oxide removal on polycrystalline w surfaces. *Applied Surface Science*, 127-129:88 – 94, 1998.

Bibliography

- [25] A. Jorio, M. S. Dresselhaus, and G. Dresselhaus. *Carbon Nanotubes*, volume 111 of *Topics in Applied Physics*. Springer Berlin, 2008.
- [26] P. Yaghoobi and A. Nojeh. Electron Emission from Carbon Nanotubes. *Modern Physics Letters B*, 21:1807–1830, 2007.
- [27] D. C. Cox, R. D. Forrest, P. R. Smith, and S. R. P. Silva. Thermionic emission from defective carbon nanotubes. *Applied Physics Letters*, 85(11):2065–2067, 2004.
- [28] Peng Liu, Qin Sun, Feng Zhu, Kai Liu, Kaili Jiang, Liang Liu, Qun-qing Li, and Shoushan Fan. Measuring the work function of carbon nanotubes with thermionic method. *Nano Letters*, 8(2):647–651, 01 2008.
- [29] Peng Liu, Yang Wei, Kaili Jiang, Qin Sun, Xiaobo Zhang, Shoushan Fan, Shufeng Zhang, Chuangang Ning, and Jingkan Deng. Thermionic emission and work function of multiwalled carbon nanotube yarns. *Phys. Rev. B*, 73(23):235412, 2006.
- [30] Yang Wei, Kaili Jiang, Xiaofeng Feng, Peng Liu, Liang Liu, and Shoushan Fan. Comparative studies of multiwalled carbon nanotube sheets before and after shrinking. *Phys. Rev. B*, 76(4):045423, Jul 2007.
- [31] Dimitrios Tasis, Nikos Tagmatarchis, Alberto Bianco, and Maurizio Prato. Chemistry of carbon nanotubes. *Chemical Reviews*, 106(3):1105–1136, 02 2006.
- [32] N. H. Tran, M. A. Wilson, A. S. Milev, J. R. Bartlett, R. N. Lamb, D. Martin, and G. S. K. Kannangara. Photoemission and absorption spectroscopy of carbon nanotube interfacial interaction. *Advances in Colloid and Interface Science*, 145(1-2):23–41, 1 2009.
- [33] Alireza Nojeh, Katerina Ioakeimidi, Samad Sheikhaei, and R. Fabian W. Pease. Photoemission from single-walled carbon nanotubes. *Journal of Applied Physics*, 104(5):054308, 2008.

- [34] Teh-Hwa Wong, Mool C Gupta, and Carlos Hernandez-Garcia. Nanosecond laser pulse-induced electron emission from multiwall carbon nanotube film. *Nanotechnology*, 18(13):135705, 2007.
- [35] W. B. Choi, D. S. Chung, J. H. Kang, H. Y. Kim, Y. W. Jin, I. T. Han, Y. H. Lee, J. E. Jung, N. S. Lee, G. S. Park, and J. M. Kim. Fully sealed, high-brightness carbon-nanotube field-emission display. *Applied Physics Letters*, 75(20):3129–3131, 1999.
- [36] Ludovic Hudanski, Eric Minoux, Laurent Gangloff, Kenneth B K Teo, Jean-Philippe Schnell, Stephane Xavier, John Robertson, William I Milne, Didier Pribat, and Pierre Legagneux. Carbon nanotube based photocathodes. *Nanotechnology*, 19(10):105201, 2008.
- [37] B. K. Choi, W. P. Kang, I. L. Davis, J. L. Davidson, S. T. Hu, and R. W. Pitz. Thermionic electron emission from chemical vapor deposition diamond by nanosecond laser heating. *Journal of Vacuum Science & Technology B: Microelectronics and Nanometer Structures*, 27(2):557–561, 2009.
- [38] A. G. Rinzler, J. H. Hafner, P. Nikolaev, P. Nordlander, D. T. Colbert, R. E. Smalley, L. Lou, S. G. Kim, and D. Tomnek. Unraveling nanotubes: Field emission from an atomic wire. *Science*, 269(5230):1550–1553, 1995.
- [39] Ayman Bassil, Pascal Puech, Lucien Tubery, Wolfgang Bacsa, and Emmanuel Flahaut. Controlled laser heating of carbon nanotubes. *Applied Physics Letters*, 88(17):173113, 2006.
- [40] Toshiyuki Nakamiya, Tsuyoshi Ueda, Tomoaki Ikegami, Kenji Ebihara, and Ryoichi Tsuda. Thermal analysis of carbon nanotube film irradiated by a pulsed laser. *Current Applied Physics*, 8(3-4):400–403, 5 2008.
- [41] Toshiyuki Nakamiya, Tsuyoshi Ueda, Tomoaki Ikegami, Fumiaki Mitsugi, Kenji Ebihara, Yoshito Sonoda, Yoichiro Iwasaki, and Ryoichi Tsuda. Effect of a pulsed nd:yag laser irradiation on multi-walled carbon nanotubes film. *Thin Solid Films*, 517(14):3854–3858, 5 2009.

- [42] M. Liu, K.L. Jiang, Q.Q. Li, H.T. Yang, and S.S. Fan. Laser-induced high local temperature in carbon nanotube. *Solid State Phenomena*, 121-123:331–336, 2007.
- [43] Kenji Hata, Don N. Futaba, Kohei Mizuno, Tatsunori Namai, Motoo Yumura, and Sumio Iijima. Water-Assisted Highly Efficient Synthesis of Impurity-Free Single-Walled Carbon Nanotubes. *Science*, 306(5700):1362–1364, 2004.
- [44] C. Zhang, S. Pisana, C.T. Wirth, A. Parvez, C. Ducati, S. Hofmann, and J. Robertson. Growth of aligned millimeter-long carbon nanotube by chemical vapor deposition. *Diamond and Related Materials*, 17(7-10):1447 – 1451, 2008.
- [45] Supriya Chakrabarti, Takeshi Nagasaka, Yuya Yoshikawa, Lujun Pan, and Yoshikazu Nakayama. Growth of super long aligned brush-like carbon nanotubes. *Japanese Journal of Applied Physics*, 45(28):L720–L722, 2006.
- [46] Anastasios John Hart, Lucas van Laake, and Alexander H. Slocum. Desktop growth of carbon-nanotube monoliths with in situ optical imaging. *Small*, 3(5):772–777, 2007.
- [47] Parham Yaghoobi, Mario Michan, and Alireza Nojeh. Middle-ultraviolet laser photoelectron emission from vertically aligned millimeter-long multiwalled carbon nanotubes. *Applied Physics Letters*, 97(15):153119, 2010.
- [48] F. J. García-Vidal, J. M. Pitarke, and J. B. Pendry. Effective medium theory of the optical properties of aligned carbon nanotubes. *Phys. Rev. Lett.*, 78(22):4289–4292, Jun 1997.
- [49] Sina Khorasani, Alireza Nojeh, and Bizhan Rashidian. Design and analysis of the integrated plasma wave micro-optical modulator/switch. *Fiber and Integrated Optics*, 21:173–191, 2002.

- [50] Zu-Po Yang, Lijie Ci, James A. Bur, Shawn-Yu Lin, and Pulickel M. Ajayan. Experimental observation of an extremely dark material made by a low-density nanotube array. *Nano Letters*, 8(2):446–451, 01 2008.
- [51] Kohei Mizuno, Juntaro Ishii, Hideo Kishida, Yuhei Hayamizu, Satoshi Yasuda, Don N. Futaba, Motoo Yumura, and Kenji Hata. A black body absorber from vertically aligned single-walled carbon nanotubes. *Proceedings of the National Academy of Sciences*, 106(15):6044–6047, 2009.
- [52] Yoichi Murakami, Shohei Chiashi, Yuhei Miyauchi, Minghui Hu, Masaru Ogura, Tatsuya Okubo, and Shigeo Maruyama. Growth of vertically aligned single-walled carbon nanotube films on quartz substrates and their optical anisotropy. *Chemical Physics Letters*, 385(3-4):298 – 303, 2004.
- [53] Don N. Futaba, Kenji Hata, Takeo Yamada, Tatsuki Hiraoka, Yuhei Hayamizu, Yozo Kakudate, Osamu Tanaike, Hiroaki Hatori, Motoo Yumura, and Sumio Iijima. Shape-engineerable and highly densely packed single-walled carbon nanotubes and their application as super-capacitor electrodes. *Nat Mater*, 5(12):987–994, 12 2006.
- [54] Parham Yaghoobi, Mehran Vahdani Moghaddam, Mario Michan, and Alireza Nojeh. Visible-light induced electron emission from carbon nanotube forests. *Journal of Vacuum Science & Technology B*, 29(2):02B104, 2011.
- [55] L. A. Bursill, Pierre A. Stadelmann, J. L. Peng, and Steven Prawer. Surface plasmon observed for carbon nanotubes. *Phys. Rev. B*, 49:2882–2887, 1994.
- [56] M.H. Upton, R.F. Klie, J.P. Hill, T. Gog, D. Casa, W. Ku, Y. Zhu, M.Y. Sfeir, J. Misewich, G. Eres, and D. Lowndes. Effect of number of walls on plasmon behavior in carbon nanotubes. *Carbon*, 47(1):162 – 168, 2009.

- [57] Richard G. Forbes. Field emission: New theory for the derivation of emission area from a fowler–nordheim plot. *Journal of Vacuum Science & Technology B*, 17(2):526–533, 1999.
- [58] Jean-Marc Bonard, Hannes Kind, Thomas Stckli, and Lars-Ola Nilsson. Field emission from carbon nanotubes: the first five years. *Solid-State Electronics*, 45(6):893 – 914, 2001.
- [59] Chun-Wei Chen and Ming-Hsien Lee. Ab initio calculations of dimensional and adsorbate effects on the workfunction of single-walled carbon nanotube. *Diamond and Related Materials*, 12(3-7):565 – 571, 2003.
- [60] Parham Yaghoobi, Mehran Vahdani Moghaddam, and Alireza Nojeh. ”heat trap”: Light-induced localized heating and thermionic electron emission from carbon nanotube arrays. *Solid State Communications*, 151(17):1105 – 1108, 2011.
- [61] Toshiyuki Nakamiya, Tsuyoshi Ueda, Tomoaki Ikegami, Fumiaki Mitsugi, Kenji Ebihara, Yoshito Sonoda, Yoichiro Iwasaki, and Ryoichi Tsuda. Effect of a pulsed nd:yag laser irradiation on multi-walled carbon nanotubes film. *Thin Solid Films*, 517(14):3854 – 3858, 2009.
- [62] Savas Berber, Young-Kyun Kwon, and David Tománek. Unusually high thermal conductivity of carbon nanotubes. *Physical Review Letters*, 84(20):4613–4616, 2000.
- [63] Jianwei Che, Tahir Çağın, and William A Goddard. Thermal conductivity of carbon nanotubes. *Nanotechnology*, 11(2):65, 2000.
- [64] P. Kim, L. Shi, A. Majumdar, and P. L. McEuen. Thermal transport measurements of individual multiwalled nanotubes. *Physical Review Letters*, 87(21):215502, 2001.
- [65] Da Jiang Yang, Qing Zhang, George Chen, S. F. Yoon, J. Ahn, S. G. Wang, Q. Zhou, Q. Wang, and J. Q. Li. Thermal conductivity of multiwalled carbon nanotubes. *Physical Review B*, 66(16):165440, 2002.

Bibliography

- [66] N. Mingo and D. A. Broido. Carbon nanotube ballistic thermal conductance and its limits. *Physical Review Letters*, 95(9):096105, 2005.
- [67] Yunfeng Gu and Yunfei Chen. Thermal conductivities of single-walled carbon nanotubes calculated from the complete phonon dispersion relations. *Physical Review Letters*, 76(13):134110, 2007.
- [68] H. Huang, C. H. Liu, Y. Wu, and S. Fan. Aligned carbon nanotube composite films for thermal management. *Advanced Materials*, 17(13):1652–1656, 2005.
- [69] I-Kai Hsu, Michael T. Pettes, Adam Bushmaker, Mehmet Aykol, Li Shi, and Stephen B. Cronin. Optical absorption and thermal transport of individual suspended carbon nanotube bundles. *Nano Letters*, 9(2):590–594, 2009.
- [70] Zhi Xu, X. D. Bai, E. G. Wang, and Zhong L. Wang. Field emission of individual carbon nanotube with in situ tip image and real work function. *Applied Physics Letters*, 87(16):163106, 2005.
- [71] Peng Liu, Yang Wei, Kaili Jiang, Qin Sun, Xiaobo Zhang, Shoushan Fan, Shufeng Zhang, Chuangang Ning, and Jingkang Deng. Thermionic emission and work function of multiwalled carbon nanotube yarns. *Physical Review B*, 73(23):235412, 2006.
- [72] Peter Hommelhoff, Yvan Sortais, Anoush Aghajani-Talesh, and Mark A. Kasevich. Field emission tip as a nanometer source of free electron femtosecond pulses. *Physical Review Letters*, 96(7):077401, 2006.
- [73] Tyler L. Westover, Aaron D. Franklin, Baratunde A. Cola, Timothy S. Fisher, and Ronald G. Reifenberger. Photo- and thermionic emission from potassium-intercalated carbon nanotube arrays. *Journal of Vacuum Science & Technology B*, 28(2):423–434, 2010.
- [74] Eric Pop, David Mann, Qian Wang, Kenneth Goodson, and Hongjie

- Dai. Thermal conductance of an individual single-wall carbon nanotube above room temperature. *Nano Letters*, 6(1):96–100, 2006.
- [75] Eric Pop, David A. Mann, Kenneth E. Goodson, and Hongjie Dai. Electrical and thermal transport in metallic single-wall carbon nanotubes on insulating substrates. *Journal of Applied Physics*, 101(9):093710, 2007.
- [76] Eric Pop, David Mann, Jien Cao, Qian Wang, Kenneth Goodson, and Hongjie Dai. Negative differential conductance and hot phonons in suspended nanotube molecular wires. *Physical Review Letters*, 95(15):155505, 2005.
- [77] Mohamed A Osman and Deepak Srivastava. Temperature dependence of the thermal conductivity of single-wall carbon nanotubes. *Nanotechnology*, 12(1):21, 2001.
- [78] S. P. Hepplestone and G. P. Srivastava. Phonon-phonon interactions in single-wall carbon nanotubes. *Physical Review B*, 74(16):165420, 2006.
- [79] D. C. Cox, R. D. Forrest, P. R. Smith, and S. R. P. Silva. Thermionic emission from defective carbon nanotubes. *Applied Physics Letters*, 85(11):2065–2067, 2004.
- [80] David Mann, Kato Y. K., Anika Kinkhabwala, Eric Pop, Jien Cao, Xinran Wang, Li Zhang, Qian Wang, Jing Guo, and Hongjie Dai. Electrically driven thermal light emission from individual single-walled carbon nanotubes. *Nature Nanotechnology*, 2(1):33–38, 01 2007.
- [81] Yang Wei, Kaili Jiang, Xiaofeng Feng, Peng Liu, Liang Liu, and Shoushan Fan. Comparative studies of multiwalled carbon nanotube sheets before and after shrinking. *Physical Review B*, 76(4):045423, Jul 2007.
- [82] P. M. Ajayan, M. Terrones, A. de la Guardia, V. Huc, N. Grobert, B. Q. Wei, H. Lezec, G. Ramanath, and T. W. Ebbesen. Nanotubes in a flash-ignition and reconstruction. *Science*, 296(5568):705, 2002.

- [83] Wonjoon Choi, Seunghyun Hong, Joel T. Abrahamson, Jae-Hee Han, Changsik Song, Nitish Nair, Seunghyun Baik, and Michael S. Strano. Chemically driven carbon-nanotube-guided thermopower waves. *Nature Materials*, 9(5):423–429, 05 2010.
- [84] Jared W. Schwede, Igor Bargatin, Daniel C. Riley, Brian E. Hardin, Samuel J. Rosenthal, Yun Sun, Felix Schmitt, Piero Pianetta, Roger T. Howe, Zhi-Xun Shen, and Nicholas A. Melosh. Photon-enhanced thermionic emission for solar concentrator systems. *Nature Materials*, 9(9):762–767, 09 2010.
- [85] David B. Geohegan, Alex A. Puretzky, Chris Rouleau, Jeremy Jackson, Gyula Eres, Zuqin Liu, David Styers-Barnett, Hui Hu, Bin Zhao, Ilia Ivanov, Kai Xiao, and Karren More. Laser interactions in nanomaterials synthesis. In Antonio Miotello and Paolo M. Ossi, editors, *Laser-Surface Interactions for New Materials Production*, volume 130 of *Springer Series in Materials Science*, pages 1–17. Springer Berlin Heidelberg, 2010.
- [86] Arun Majumdar. Thermoelectricity in semiconductor nanostructures. *Science*, 303(5659):777–778, 2004.
- [87] Lee A. DuBridge. A further experimental test of fowler’s theory of photoelectric emission. *Phys. Rev.*, 39:108–118, 1932.
- [88] J. H. Bechtel. Heating of solid targets with laser pulses. *Journal of Applied Physics*, 46:1585–1593, 1975.
- [89] Parham Yaghoobi, Mehran Vahdani Moghaddam, and Alireza Nojeh. Broadband-light-induced thermionic electron emission from arrays of carbon nanotubes using laser pointers. In *The 55th International Conference on Electron, Ion, and Photon Beam Technology and Nanofabrication*, Las Vegas, USA, May 2011.
- [90] Parham Yaghoobi, Mehran Vahdani Moghaddam, and Alireza Nojeh. Increasing the current density of light-induced thermionic electron emis-

Bibliography

- sion from carbon nanotube arrays. In *The 24th International Vacuum Nanoelectronics Conference*, Wuppertal, Germany, July 2011.
- [91] Md. K. Alam, P. Yaghoobi, and A. Nojeh. Unusual secondary electron emission behavior in carbon nanotube forests. *Scanning*, 31(6):221–228, 2009.
- [92] M. Dahmardeh, W. Khalid, M.S. Mohamed Ali, Y. Choi, P. Yaghoobi, A. Nojeh, and K. Takahata. High-aspect-ratio, 3-d micromachining of carbon-nanotube forests by micro-electro-discharge machining in air. In *Micro Electro Mechanical Systems (MEMS), 2011 IEEE 24th International Conference on*, pages 272 –275, 2011.
- [93] A. Bsoul, M.S. Mohamed Ali, and K. Takahata. Piezoresistive pressure sensor using vertically aligned carbon-nanotube forests. *Electronics Letters*, 47(14):807 –808, 2011.
- [94] Y. Kojima, K. Kasuya, K. Nagato, T. Hamaguchi, and M. Nakao. Solid-phase growth mechanism of tungsten oxide nanowires synthesized on sputtered tungsten film. *Journal of Vacuum Science & Technology B: Microelectronics and Nanometer Structures*, 26:1942–1947, 2008.